Phosphorene: from theory to applications

Alexandra Carvalho[1], Min Wang[2]*, Xi Zhu[3], Aleksandr S. Rodin[1], Haibin Su[3,4,5] and Antonio H. Castro Neto[1]*

Abstract | 2D materials are the focus of an intense research effort because of their unique properties and their potential for revealing intriguing new phenomena. Phosphorene, a monolayer of black phosphorus, earned its place among the family of 2D semiconductor materials when recent results unveiled its high carrier mobility, high optical and UV absorption, and other attractive properties, which are of particular interest for optoelectronic applications. Unlike graphene, phosphorene has an anisotropic orthorhombic structure that is ductile along one of the in-plane crystal directions but stiff along the other. This results in unusual mechanical, electronic, optical and transport properties that reflect the anisotropy of the lattice. This Review summarizes the physical properties of phosphorene and highlights the recent progress made in the preparation, isolation and characterization of this material. The role of defects and doping is discussed, and phosphorene-based devices are surveyed; finally, the remaining challenges and potential applications of phosphorene are outlined.

[1]Centre for Advanced 2D Materials and Graphene Research Centre, National University of Singapore, Singapore 117542, Singapore.
[2]Faculty of Materials and Energy, Southwest University, Chongqing 400715, China.
[3]Division of Materials Science, Nanyang Technological University, 50 Nanyang Avenue, Singapore 639798, Singapore.
[4]Institute of Advanced Studies, Nanyang Technological University, 60 Nanyang View, Singapore 639673, Singapore.
[5]Energy Research Institute, Tianneng Group, Huaxi Industrial Function Zone, Changxing County, Zhejiang 313100, China.
**These authors contributed equally to this work.*

Correspondence to H.S. and A.H.C.N.
haibin.su.hbsu@gmail.com; phycastr@nus.edu.sg

Article number: 16061
doi:10.1038/natrevmats.2016.61
Published online 31 Aug 2016

Black phosphorus, along with graphite, is one of the few layered crystals that are constituted by a single atomic species. Despite being its most stable allotrope, this high density phase was synthesized centuries after the initial discovery of the element phosphorus.

The first appearance of phosphorus in historical records dates back to around 1046–771 BC in ancient China, where the spontaneous combustion of P_2H_4 was described in "The Book of Odes and Hymns" (诗经). However, elemental phosphorus in its molecular form, referred to as white phosphorus[1], was only isolated in 1669 by Hennig Brand. In 1914, whilst investigating the effects of high pressure on white phosphorus, Percy Bridgman observed a phase transition and named the new allotrope black phosphorus[2]. Even though it was discovered last, under normal conditions this new phase is more thermodynamically stable than white and red phosphorus[3–6]. In total, at least five crystalline polymorphs of phosphorus and several amorphous forms have been synthesized as of today[6], and other phases have been predicted theoretically[7–9].

Since the late 1960s, the rise of interest in superconductivity drove attention to the rich phase diagram of phosphorus[10–14]. It was found that this element becomes superconducting with a critical temperature, T_c, of 4–10 K, presumably when it is in its high-pressure cubic and rhombohedral forms[10,14]. This led to a development of high-pressure routes for black phosphorus growth. However, as a semiconductor, black phosphorus attracted little interest as a result of its diminutive bandgap (0.3 eV) and the difficulty of controlling the material quality[5].

The discovery of graphene brought forth a rapid development of exfoliation and other thin-layer processing techniques, leading to a renewed interest in black phosphorus. In 2014, theoretical and experimental works revealing the electronic properties of monolayer or few-layer black phosphorus were published[15–17]. The results, showing a direct bandgap and high carrier mobility (TABLE 1), stimulated the beginning of a new chapter in research on what came to be named phosphorene[17]: that is, monolayer black phosphorus. Curiously, this name does not reflect the chemical nature of the material, which has no sp^2 bonds; instead, it comes from its conceptual similarity to graphene — the IUPAC name should be 2D phosphane[18].

Although phosphorene, as a 2D material, became a field of study very recently, there are already several reviews on the subject[19–21] covering material properties, fabrication and devices. This Review provides an updated account of phosphorene physics and applications, relating them to the underlying theory.

Material properties

Crystal structure. Phosphorus chemistry can be understood by considering the white phosphorus P_4 molecule. Its four atoms form a tetrahedron with six single bonds, so that every phosphorus atom forms three

© 2016 Macmillan Publishers Limited, part of Springer Nature. All rights reserved.

bonds with its neighbours. These bonds result from the 3*p* atomic orbitals, but in this tetrahedral configuration the bonds cannot adopt a 90° angle, as pure 3*p* orbitals would. Rather, the structure is stabilized by arc-like bonds[22,23]. Hence, the white phosphorus molecule is known for its instability[6].

By contrast, in phosphorene, P_4 units are joined to form continuous layers (BOX 1). This requires the breaking of individual P_4 bonds to form sp^3 bonds with bond angles of 96.34° and 103.09° — much closer to the angle of a perfect tetragonal structure, 109.5°— resulting in increased stability of the crystal structure. The remaining lone pairs point out of the layers at an angle of approximately 45° with respect to the plane and are responsible for the puckering of the structure. Because of the different bond angles, each atom has two neighbours at 2.224 Å and a third one at 2.244 Å (REF. 24). Based on the similarity with graphene, the *y* axis is usually named the zigzag direction, whereas the *x* axis is referred to as the armchair direction.

The lattice constants of bulk black phosphorus have been determined using time-of-flight neutron powder diffraction[25], yielding 4.374, 3.313, and 10.473 Å for *a*, *b* and *c*, respectively. However, the different magnitudes of the covalent intralayer bonds and of the weak interlayer bonds, and the anisotropy of the in-plane bonding geometry, make it very difficult to accurately reproduce these lattice parameters with first principles modelling[16,26].

The structure of phosphorene is orthorhombic (BOX 1). This, together with its characteristic puckering, sets phosphorene aside from most of 2D materials, such as graphene, boron nitride (BN) and transition metal dichalcogenides (TMDCs), all of which have hexagonal planar structures. The puckering of phosphorene results in unusual mechanical properties, such as a negative Poisson's ratio (−0.027) for the *z* direction when the stretch and compression occur in the *y* direction[27], which means that stretching the material in a direction increases the size of the sample in the transverse direction (Supplementary information S1 (table)).

Electronic band structure. The electronic band structure of monolayer, few-layer and bulk black phosphorus exhibits a direct bandgap, ranging from ~0.3 eV (bulk) to ~2.0 eV (monolayer)[28].

A comparison between the band structure of the monolayer, bilayer and trilayer (FIG. 1a) reveals a redshift of the bandgap with the increasing number of layers, accompanied by a concurrent splitting of the bands. By contrast, the band dispersion remains nearly unperturbed. The bandgap is at the Γ point of the Brillouin zone for both monolayer and multilayers. However, it should be noted that for monolayer phosphorene the valence band top is nearly flat and, therefore, the possibility that its maximum is slightly off the Γ point cannot be excluded neither on the basis of symmetry considerations nor from the results of density functional theory calculations[16,29]. However, if the off-centred maximum exists, it is probably too shallow to be measured at room temperature. The bandgap is also direct (at Z) for bulk black phosphorus, as confirmed by angle-resolved photoemission spectroscopy (ARPES) measurements[15] (FIG. 1b). To date, there are no ARPES measurements for few-layer or monolayer samples.

The presence of a direct bandgap for any number of layers sets phosphorene apart from MoS_2 and WS_2, which display an indirect-to-direct bandgap transition upon going from bulk to monolayer[28]. However, it should be noted that several less-known chalcogenides, such as ReS_2, TiS_3 and InSe, have a direct bandgap for both monolayer and multilayers. From the point of view of optoelectronic applications, the presence of a direct bandgap independently from the number of layers constitutes an advantage, because it is easier to fabricate stable devices using few-layer rather than monolayer phosphorene. Another reason why phosphorene is interesting in the context of optoelectronic applications is the large portion of the electromagnetic spectrum covered by the thickness-dependent bandgaps, going from the visible down to the middle infrared — below the spectral region covered by the most common semiconducting TMDCs. The bandgap as a function of thickness calculated using the GW method in the G_0W_0 approximation, one of the most reliable first-principles electronic structure methods for bandgap determination, is shown in FIG. 1c. Experimental and theoretical values for the bandgap are reported in the Supplementary information S2 (table). Because the exciton binding energy is very large in 2D materials (discussed further below), a direct comparison between electron bandgaps — such as the one obtained from G_0W_0 calculations and from band

Table 1 | **Properties of phosphorene compared with those of other 2D materials**

2D material	Crystal class	Electronic structure	Bandgap (eV)*	Mobility ($cm^2 V^{-1} s^{-1}$)
Graphene	Hexagonal	Semimetal	NA	2,000–5,000 (supported; experimental values)[130] 200,000 (freestanding; experimental value)[131]
TMDCs (MoS_2)	Hexagonal	Semiconductor	From 1.29 for bulk (indirect) to 1.96 for monolayer (direct)[132]	<320 for electrons, <270 for holes (theoretical values)[133]
Phosphorene	Orthorhombic	Semiconductor	From 0.3 for bulk (direct) to 1.75 for monolayer (direct)	<10,000–26,000 (monolayer; theoretical values) 400–4,000 (few-layer; experimental values)
h-BN	Hexagonal	Insulator	5.971 (direct)[134]	–

h-BN, hexagonal boron nitride; NA, not available; TMDCs, transition metal dichalcogenides. *Bandgap values are all from experimental sources.

© 2016 Macmillan Publishers Limited, part of Springer Nature. All rights reserved.

structure calculations — and the bandgaps measured in optical experiments can be misleading. For example, the difference between the measured optical bandgap in FIG. 1c and the value obtained from the Bethe–Salpeter equation can be attributed to the fact that the theoretical value was calculated in vacuum, whereas the experimental value was obtained from measurements on a sample supported on a dielectric substrate.

Optical spectra. Because phosphorene is highly anisotropic, it displays dichroism — that is, light rays with different polarization are absorbed at different rates[30]. Dichroism is especially marked for frequencies close to that corresponding to the bandgap energy, because only light with a component of the polarization along the armchair direction is absorbed; this happens because the specific symmetry of the electron wave function in the conduction and valence bands forbids absorption of light polarized along the zigzag direction.

Box 1 | **Symmetry**

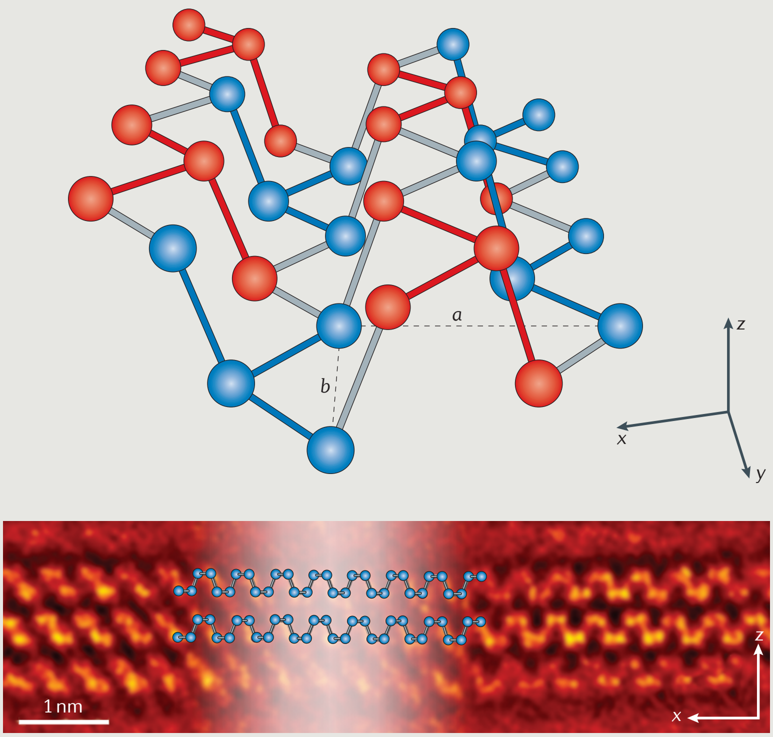

The base-centre orthorhombic lattice of bulk black phosphorus belongs to the space group *Cmca* (64, D_{2h}^{18}), whose factor group is isomorphic to the point group *mmm* (D_{2h}). This point group contains the following symmetry operations in addition to identity: inversion (*i*), π rotation around the *y* axis (C_{2y}), reflection with respect to the *xz* plane (R_y) and four operations followed by a translation $t = (a_x/2, a_y/2)$ (tC_{2x}, tC_{2z}, tR_x, tR_z)[31]. Monolayer phosphorene belongs to the space group *Pbmn* (53, D_{2h}^{7}). For few-layer systems, the symmetry is different for an odd and even number of layers (D_{2h}^{7} and D_{2h}^{11}, respectively), with the even-numbered layer stacks lacking inversion symmetry[43]. The structure of phosphorene is represented in the figure, and the lattice constants *a* and *b* are indicated (top panel).

The most common layer stacking in black phosphorus is AB. The bottom panel shows an aberration-corrected transmission electron microscopy image with an overlaid ball-and-stick atomic model[121].

Indeed, the direction-dependent optical absorption rate for a transition is proportional to the square of the dipole matrix elements $\langle f|\hat{p}_{x,y}|i\rangle$, where $\hat{p}_{x,y}$ is the momentum operator, and $|i\rangle$ and $|f\rangle$ are the initial (occupied) and final (unoccupied) states, respectively. For monolayer phosphorene, the matrix element of $\hat{p}$ between the top of the valence band and the bottom of the conduction band is finite, allowing the electronic transition. By contrast, the transition due to *y*-polarized light is forbidden by symmetry. The strength of the optical transitions between individual bands in monolayer phosphorene is shown in FIG. 2a, and the modelled absorption spectra for *x* and *y* excitation are shown in FIG. 2b,c, respectively.

The selection rules for the optical conductivity are the same as for the optical absorption. The optical conductivity tensor of few-layer phosphorene, calculated using the Kubo formula within an effective low-energy Hamiltonian, can be found in REF. 31.

Because the optical properties of phosphorene are very anisotropic, they can be used to determine the direction of the crystallographic axes. The polar representations of the absorption and extinction coefficient are shown in FIG. 2c for a thick multilayer sample. Its dumbbell shape is oriented along the main crystallographic axis. In addition, in bulk black phosphorus, there is a giant increase of the optical conductivity starting at about 3 eV, which originates in a band-nesting region[30,32]. Phosphorene can thus be used as a photodetecting material with high responsivity in the UV region (as discussed later).

Excitons and photoluminescence. In phosphorene, similarly to other monolayer semiconductors, reduced dimensionality and reduced screening of the Coulomb attraction lead to a fairly high exciton binding energy of 800 meV (REF. 28) (BOX 2). Indeed, polarization-resolved photoluminescence measurements report highly anisotropic and tightly bound excitons in monolayer phosphorene, and deduce an exciton binding energy of 900 ± 100 meV from the energy difference between the excitonic emission peak and the quasiparticle bandgap, which is defined as the energy position at which the absorption increase rate is largest[33]. A high exciton binding energy stabilizes excitons and trions (charged excitons) against thermal fluctuations; it increases the lifetime of these composite particles and is thus desirable for applications such as light transport by trions and optically driven quantum computing.

Phosphorene exhibits a charge carrier effective mass anisotropy, with lighter effective masses along the armchair direction and heavier effective masses along the zigzag direction (Supplementary information S3 (table)). As a consequence, excitons in phosphorene are characterized by a strong spatial anisotropy, with the wave function extended along the armchair direction[33,34]. Because this anisotropy arises as a consequence of the directional mass dependence, it can be observed also in multilayer phosphorene. However, adding extra layers introduces additional screening and reduces the binding energy. The spatial distribution of the wave functions of the first

© 2016 Macmillan Publishers Limited, part of Springer Nature. All rights reserved.

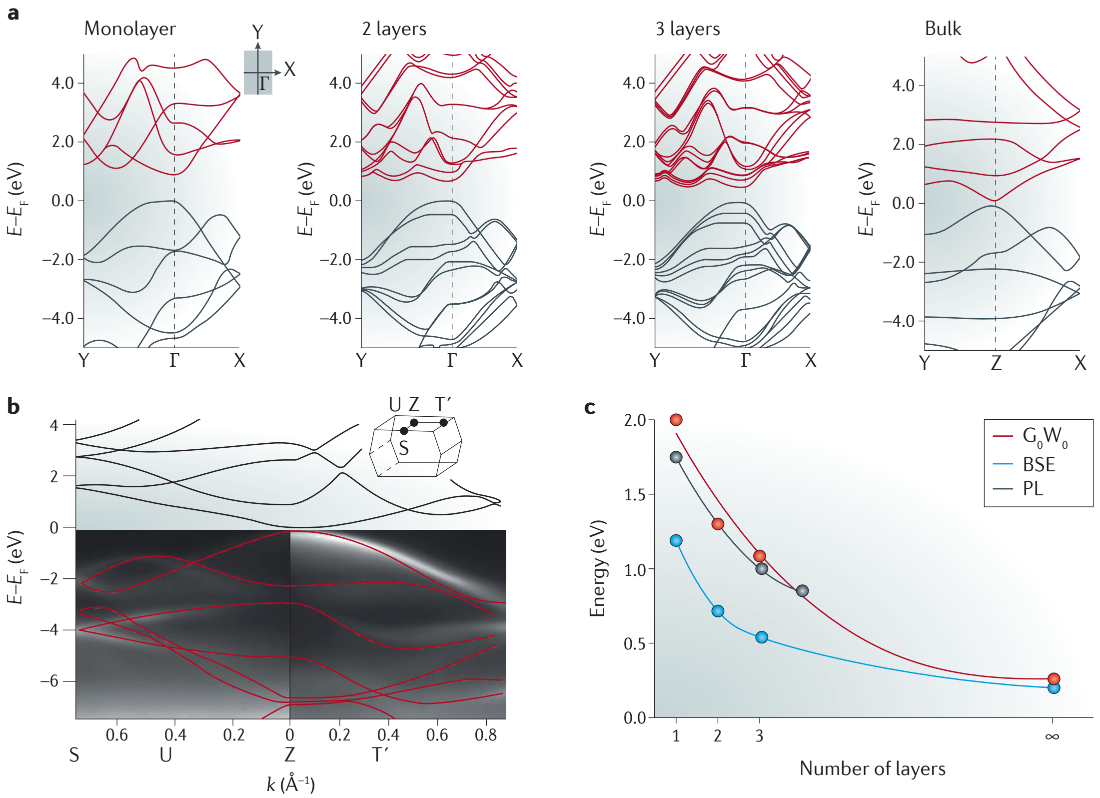

Figure 1 | **Band structure of phosphorene. a** | Band structures obtained by density functional theory for one, two and three layers of phosphorene, and for bulk black phosphorus, calculated with the PBEsol functional[125]. $\Gamma = (0, 0)$ denotes the centre of the 2D Brillouin zone. **b** | Angle-resolved photoemission spectroscopy spectra compared with bands obtained with density functional theory calculations based on a Heyd–Scuseria–Ernzerhof functional for bulk black phosphorus. The inset shows the first 3D Brillouin zone of black phosphorus. **c** | The bandgap as a function of the number of layers, theory (G_0W_0 and Bethe-Salpeter equation (BSE)[28]) and experiment (photoluminescence (PL)[38]). E_F, Fermi energy; *k*, wave vector. Panel **a** is reproduced with permission from REF. 31, American Physical Society. Part **b** is from REF. 15, Nature Publishing Group. Part **c** is adapted with permission from REF. 28, American Physical Society.

bound exciton in monolayer phosphorene is shown in FIG. 2d. Owing to the selection rules discussed in the previous section, the excitons are optically active only when the incident light is polarized along the armchair direction. The excitonic structure can be affected by the number of layers: in three-layer phosphorene, holes are located in a monolayer, whereas the electronic distributions extend to the other two layers. In contrast to other layered materials, the bulk exciton binding energy is substantially smaller than the monolayer value — in bulk black phosphorus it is around 30 meV, comparable to the value observed in other bulk semiconductors[35,36]. The reason for this reduction in binding energy is the screening arising from the strong interlayer interactions in black phosphorus.

The photoluminescence spectra of few-layer phosphorene are thickness-dependent (FIG. 2e) and show a redshift of the photoluminescence peaks with an increasing number of layers[37] (FIG. 1c). It is interesting to note that the photoluminescence from bi- to five-layer phosphorene is much more intense than that of the silicon substrate underneath, which is due to the direct nature of the bandgap in phosphorene. The photoluminescence peak intensity and the quantum efficiency increase with the number of layers[37].

There is some variability in the energies of the photoluminescence peaks reported in different studies for few-layer phosphorene[33,37–40] and, in particular, for the monolayer (the values range between 1.31 and 1.75 eV). This can be partially accounted for by the fact that the exciton binding energy exhibits a strong dependence on the external dielectric environment and is reduced to about 400 meV in the presence of a SiO_2 substrate[34,40]. However, it is also possible that the monolayer has been misidentified in some of the earlier works.

Trions have also been detected in phosphorene, with a binding energy of 100 meV (on a SiO_2 substrate), a value several times higher than that observed in semiconducting TMDCs[39].

Charge transport. The large carrier mobility observed in phosphorene is one of the factors that drew attention to this material over the past years and has been a driving force for the improvement of preparation and encapsulation methods. Typically, the mobility increases smoothly with an increasing number of layers up to a thickness of about 10 nm, reaching values exceeding 1,000 $cm^2 V^{-1} s^{-1}$ along the *y* direction (see TABLE 1 for a comparison with other materials)[15]. The comparison

© 2016 Macmillan Publishers Limited, part of Springer Nature. All rights reserved.

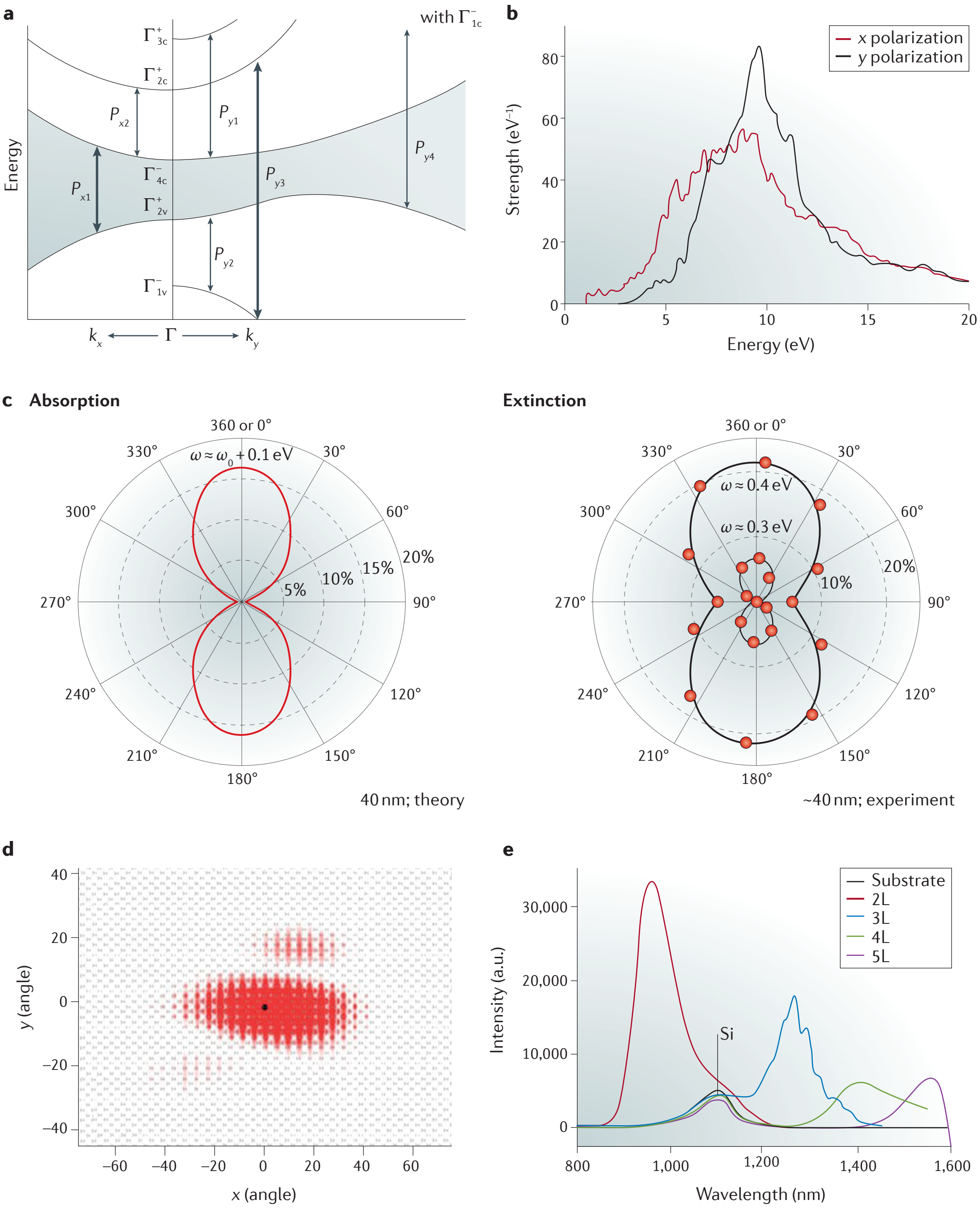

Figure 2 | **Optical properties of phosphorene. a** | Diagram showing the dipole-allowed transitions in monolayer phosphorene. Thinner arrows indicate weaker transitions. Only the relevant bands are represented. P_i represents the component of the momentum involved in each transition, and Γ is the origin of the reciprocal space. **b** | The dipole response (optical absorption) of monolayer phosphorene nanostructures to an impulse excitation polarized along the *x* and *y* directions, respectively. **c** | A polar representation of the absorption coefficient for 40-nm-thick black phosphorus for normal incident light with excitation energies greater than the bandgap (ω_0) is shown on the left. A polar representation of the experimental extinction spectra obtained from Fourier transform infrared spectroscopy for 40-nm-thick black phosphorus on a SiO_2 substrate is shown on the right. The polar representation of the experimental differential extinction coefficient for polarized light, $Z(\omega) = 1 - T/T_0$, where *T* is the extinction coefficient and T_0 is its reference value, has a dumbbell-like shape with the form $a\sin(2\theta) + b\cos(2\theta)$, where θ is the polarization angle, and *a* and *b* are constants. **d** | Lowest energy exciton wavefunctions in monolayer phosphorene. **e** | Photoluminescence spectra measured on samples with different numbers of phoshorene layers. a.u. arbitrary units. $k_{x,y}$, wave vectors along the *x* and *y* directions, respectively. Part **a** is adapted with permission from REF. 29, American Physical Society. Part **b** is adapted with permission from REF. 118, Springer-Verlag. Part **c** is adapted with permission from REF. 31, American Physical Society. Part **d** is adapted with permission from REF. 28, American Physical Society. Part **e** is adapted with permission from REF. 37, American Chemical Society.

© 2016 Macmillan Publishers Limited, part of Springer Nature. All rights reserved.

of this value with the theoretical limit for phonon-limited carrier mobility shows that there is still room for improvement: for holes, the mobility may reach values of up to 10,000–26,000 $\mathrm{cm^2\,V^{-1}\,s^{-1}}$ along the y direction for the monolayer and up to 4,800–6,400 $\mathrm{cm^2\,V^{-1}\,s^{-1}}$ for thick (five-layer) phosphorene[26].

Quantum oscillations. For a material to become viable for technological applications, it is crucial that it meets certain benchmarks concerning its quality. One metric that can be used to assess the purity of a material is the presence of quantum effects. The recent observation of quantum oscillations in phosphorene is proof of the high crystal quality and purity that has been achieved. The application of a magnetic field to a 2D electron gas leads to the formation of Landau levels; in sufficiently clean systems, sweeping the Fermi level through these quantized Landau levels results in an oscillatory behaviour of the resistance. Because the spacing between the Landau levels is quite small, low temperatures are required to observe this phenomenon. Recently, such oscillating resistance was measured in encapsulated phosphorene[41,42]. The presence of a Zeeman splitting at magnetic fields $B > 8\mathrm{T}$ was also revealed[42]. The observation of such fine details serves as a testament to the cleanliness of the encapsulated system, because these features are easily concealed by disorder. Indeed, room-temperature mobility in few-layer phosphorene is very high: it is reported to be around 400 $\mathrm{cm^2\,V^{-1}\,s^{-1}}$ and to increase at lower temperatures — up to 4,000 $\mathrm{cm^2\,V^{-1}\,s^{-1}}$ at 1.5 K (REF. 42). For field-effect transistors (FETs) based on phosphorene, the on/off ratio exceeds 10^5, which is very promising for potential electronic applications.

Box 2 | 2D Electrostatic potential

In polarizable 2D materials, the Coulomb interaction is modified; although at long-range distances it retains its $1/r$ behaviour, for smaller distances the potential well is logarithmic. This gentler divergence at small r should not be neglected, because it leads to a substantial reduction of the binding energy.

The full form of the potential for a material of polarizability ζ, positioned on top of a substrate with a dielectric constant ε, is reminiscent of the Keldysh potential for thin dielectric slabs and is given by

$$V_{2D}(r) = \frac{\pi}{2\kappa r_0}\left[H_0\left(\frac{r}{r_0}\right) - Y_0\left(\frac{r}{r_0}\right)\right]$$

where $r_0 = 2\pi\zeta/\kappa$, with $\kappa = (1+\varepsilon)/2$, and H_0 and Y_0 are Struve and Bessel functions, respectively. The image[122] illustrates the reduced screening of the Coulomb attraction between an electron and hole in a 2D material compared with the attraction in a 3D material. This reduced screening gives rise to strongly bound excitons in 2D materials.

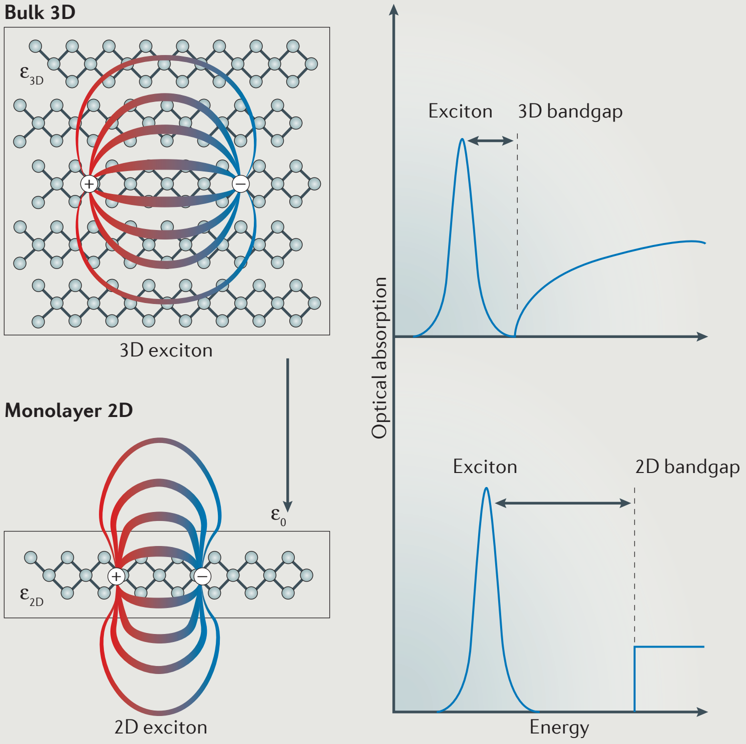

Because of the highly anisotropic band dispersion in phosphorene, the mass that determines the Landau level spacing is the geometric average of m_x and m_y. This is just one of the peculiarities associated with a direction-dependent mass, and highly clean phosphorene systems provide an excellent platform for investigating other phenomena associated with mass anisotropy.

Plasmons. The anisotropic band dispersion of phosphorene has profound effects not only on the electronic mobility, but also on the polarization of the material. Because the polarization function controls collective electronic excitations, plasmons are expected to exhibit a strong direction dependence. Although the full phosphorene Hamiltonian is rather complicated, the plasmonic dispersion can be obtained using a single anisotropic band with the random phase approximation[16,29,31].

What makes phosphorene stand out among other 2D materials is the fact that the onset of the Landau damping — a phenomenon occurring when plasmons can dissociate by recombining electrons and holes whilst preserving energy and momentum — is direction-dependent. If a plasmonic branch in the energy-momentum space is located in the region where the band structure prohibits this recombination, according to the random phase approximation, plasmons have an infinite lifetime. In reality, of course, there are higher-order decay mechanisms, but the random phase approximation describes the plasmonic behaviour to the leading-order approximation. In simpler terms, the system anisotropy can be used as a means to restrict or permit the propagation of plasmons.

Phonons. The phonon band structure of monolayer phosphorene is shown in FIG. 3a. Having four atoms per unit cell, phosphorene has a total of twelve phonon branches, three acoustic and nine optical[43]. A complete list of the vibrational modes of phosphorene is given in the Supplementary information S4 (table).

Because the Raman tensor of the B_{3g} mode contains only yz elements, it vanishes if the incident and detected light do not contain both y- and z-polarized components. The polarization-dependent Raman measurement of

© 2016 Macmillan Publishers Limited, part of Springer Nature. All rights reserved.

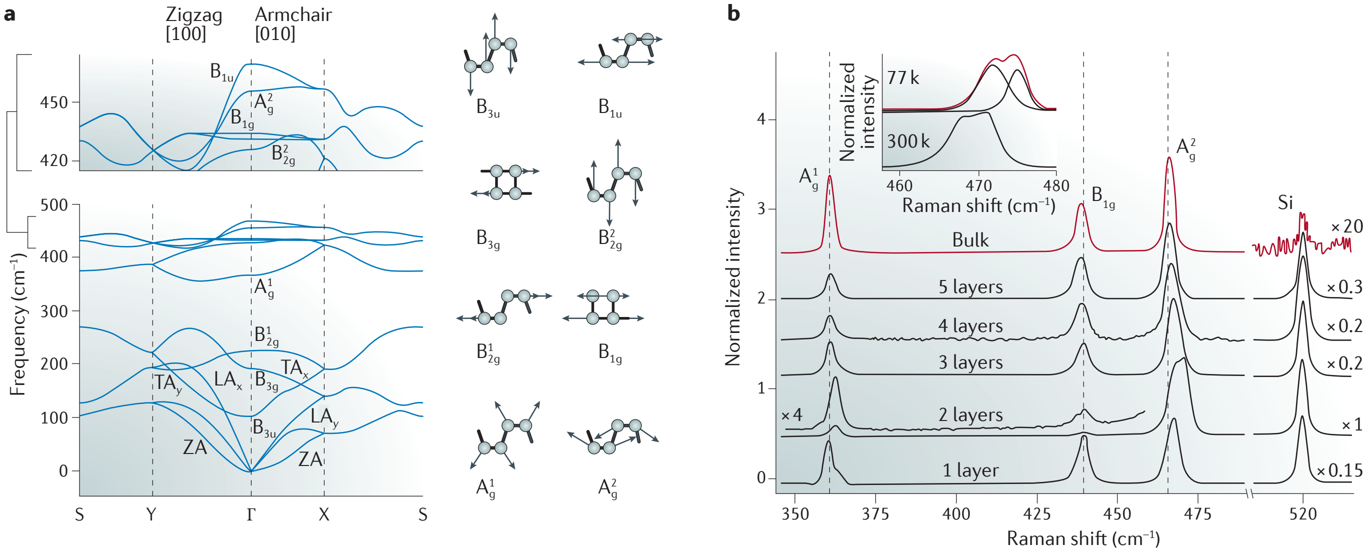

Figure 3 | **Phonon band structure and Raman spectra of phosphorene. a** | Phonon band structure of monolayer phosphorene. A close-up view of the higher energy optical modes is shown in the top left panel. The schematic illustrations on the right show the vibrating patterns of the optical modes. Γ = (0, 0) denotes the centre of the 2D Brillouin zone, and the points X, Y and S have coordinates (1, 0), (0, 1) and (1, 1), respectively (see Supplementary information S4 (table) for a conversion of the symmetry notation for different coordinate settings). **b** | Raman spectra measured at a wavelength of λ = 532 nm at 300 K on phosphorene samples with different thicknesses. Spectra are shifted for clarity and scaled by the factor shown next to each spectrum. The inset shows a close-up of the spectra for the two-layer sample. Part **a** is reproduced with permission from REF. 126, Wiley-VCH. Part **b** is from REF. 18, Nature Publishing Group.

few-layer phosphorene flake can thus provide a fast and precise determination of its crystalline orientation[34,37,44]. Unfortunately, the frequency of the three most intense, high-frequency Raman bands is weakly dependent on the number of layers[18] (FIG. 3b), and the Raman peak position is not an unambiguous signature of the layer number because its shift can be caused by other factors, such as zigzag strain[45].

Heat transport and thermoelectric effect. For thermoelectric applications, such as thermoelectric generators and thermoelectric coolers, a high Seebeck coefficient, high electrical conductivity and low thermal conductivity are desirable (BOX 3). Both bulk black phosphorus and phosphorene have a high Seebeck coefficient ($S = 335 \pm 10\,\text{V}\,\text{K}^{-1}$ for p-type black phosphorus at room temperature[46]) and comparable thermal conductivities. However, in monolayer phosphorene the preferred directions for heat and charge conduction are orthogonal, giving rise to an enhanced thermoelectric effect.

As already mentioned for monolayer phosphorene, near the Γ point the effective masses for both electrons and holes are larger along the zigzag direction than along the perpendicular direction. In addition, the phonon-limited electron and hole mobilities are also anisotropic. As a result, an anisotropic conductance, about one order of magnitude larger along the armchair direction than along the zigzag direction, is observed across all doping levels[47].

By contrast, thermal conductivity is higher along the zigzag direction[47–49]. Although there is some variation in the reported thermal conductivities[48,49], thermal measurements by micro-Raman spectroscopy of zigzag and armchair conductivity for monolayer phosphorene give ~18 and $12\,\text{W}\,\text{m}^{-1}\,\text{K}^{-1}$, respectively; both values increase with the thickness of the sample[49].

As a result, monolayer phosphorene is predicted to be an excellent thermoelectric material. The maximum figure of merit, ZT (BOX 3), has been theoretically predicted to be 0.2–0.7 in doped phosphorene at a low temperature[50], but at 500 K it can reach 2.5 (REF. 47). In nanoribbons, the value of ZT can be even higher[47,51]. The high-temperature ZT of 2.5, which is comparable to or even in excess of some of the highest values of ZT (found in Pb chalcogenide alloys[52]) makes phosphorene attractive for industrial applications.

Superconductivity. It is well known that the high pressure phase of phosphorus, cubic phosphorus, is superconductive. Its T_c varies non-monotonically with pressure, peaking at 9.5–10.7 K at about 30 GPa (REF. 13). A calculation based on the linear muffin-tin orbital method reproduced the variation of T_c with pressure and correlated the change in behaviour with the appearance of a new piece of Fermi surface[11]. However, this change was predicted to occur at a much higher pressure than that observed experimentally. More recently, *ab initio* calculations taking into account the electron–phonon interactions only found a decrease of T_c with increasing pressure[12]. Therefore, the reason behind the increase of T_c with pressure remains unexplained. One possibility is that this behaviour is not intrinsic to the cubic phase. In fact, below 15 K, T_c depends on the path taken on the temperature–pressure phase diagram[53]: this hysteresis has been attributed to the coexistence of black and rhombohedral phosphorus, and to the presence of dislocations in the mixed system.

© 2016 Macmillan Publishers Limited, part of Springer Nature. All rights reserved.

Monolayer phosphorene has also been presented as a potential superconductor, following a recent computational study[54]. Although it is a semiconductor, it can in principle be made into an n-type material, and T_c would increase with the doping concentration, reaching a value of about 10 K for a quite large doping of 0.4 electrons per cell. Moreover, it was also found that bilayer phosphorene can be transformed by inserting lithium atoms from a direct semiconductor into a typical Bardeen–Cooper–Schrieffer (BCS)-like superconductor, with a T_c of 16.5 K (REF. 55).

Synthesis

Synthesis of black phosphorus. Black phosphorus was first synthesized by Bridgman[2,3]. The original method required the application of high pressure (1.2–1.3 GPa) to white phosphorus at 200 °C (FIG. 4a,b). Keyes improved Bridgman's method by providing the ability to control the crystallinity of the sample[5]. In the meantime, another method for the production of black phosphorus had been introduced based on the direct transformation of red phosphorus at room temperature, which required an even higher pressure of 8.0 GPa (REF. 56). Later, it was found that white phosphorus was soluble in liquid bismuth and that black phosphorus could be recovered by keeping the solution at 300–400 °C for 20 hours and then slowly cooling it down to room temperature[57] (FIG. 4c). Even though this method removed the need for high pressure, it remained unsatisfactory because of the toxicity of bismuth and the very low throughput (the size of the obtained crystals was 5 × 0.1 × 0.07 mm^3, smaller than that achievable by high-pressure routes).

Box 3 | Seebeck effect and thermoelectric figure of merit

The Seebeck coefficient, *S*, of a material is a measure of the magnitude of the thermoelectric voltage induced in response to a temperature gradient arising because of the Seebeck effect. It can be defined by $\mathbf{J} = -\sigma\nabla V - \sigma S\nabla T$, where $\mathbf{J}$ is the current density, σ is the electrical conductivity, V is the induced voltage and T is the temperature. The energy production efficiency of a thermoelectric material is characterized by the dimensionless figure of merit:

$$ZT = \frac{\sigma S^2 T}{\lambda}$$

Thermoelectric materials with a *ZT* above two are usually engineered by nanostructuring[123]. An exception is SnSe, which is isoelectronic with phosphorene and adopts a similar structure[124]. The figure shows the *ZT* of phosphorene in the context of the evolution of thermoelectric materials. Data predating 2013 is from REF. 123. Data for SnSe is from REF. 124.

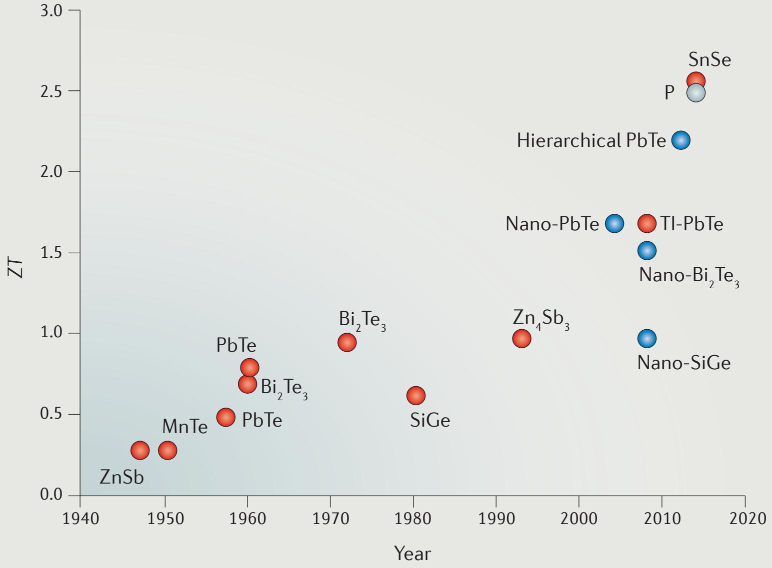

In 2007, it was found that black phosphorus could be prepared from red phosphorus at a low pressure and at 873 K by adding small quantities of gold, tin and tin(IV) iodide[58] (FIG. 4d). This process produces samples with good crystallinity but reportedly takes 10–70 hours[59]. Thus, the development of a safe, high-throughput and scalable route for the production of black phosphorus remains one of the bottlenecks impeding the use of phosphorene for applications.

Exfoliation. The exfoliation energy of black phosphorus is found to be −151 meV per atom on the basis of multilevel quantum chemical calculations[60], substantially larger than that of graphite, which accounts for the relative difficulty in exfoliating black phosphorus. This is associated with a non-negligible electronic density overlap between the layers[61] — it is a matter of debate whether the interlayer bonding can be classified as van-der-Waals type.

Microcleavage of bulk black phosphorus crystals using the 'scotch-tape' method, similar to that used for graphene and TMDCs, can yield high-quality mono- and few-layer phosphorene samples, which are ideal for fundamental research. However, only small-size crystals can be produced through this process.

Liquid exfoliation, consisting of ultrasonic exfoliation of black phosphorus immersed into a solvent, is better suited for large-scale production. The resulting phosphorene is produced in liquid phase and can be size-separated by centrifugation, and processed by liquid processing methods such as spin coating. Black phosphorus can be exfoliated using several solvents. Among anydrous solvents, aprotic and polar solvents, such as dimethylformamide (DMF)[62], dimethyl sulfoxide (DMSO)[62], *N*-methyl-2-pyrrolidone (NMP)[63,64] and *N*-cyclohexyl-2-pyrrolidone (CHP)[65], have been found to produce the most uniform and stable dispersions. Aqueous solutions can also be used with the addition of stabilizing surfactants together with deoxygenated water to avoid exposure of phosphorene to oxidizing species[66]. Liquid exfoliation can yield phosphorene with thicknesses down to the monolayer limit. After exfoliation, samples can be thinned in a plasma (Ar^+), a process that preserves the crystal quality, as demonstrated by Raman measurements[67].

Degradation. The lone pairs of phosphorus atoms at the surface of phosphorene are preferential chemisorption sites for oxygen[68–71], leading to the formation of oxygen defects and making the surface of phosphorene hydrophilic, ultimately resulting in the formation of a mixture of oxide and phosphoric acid. After a few hours of exposure to air, a significant increase in the surface

© 2016 Macmillan Publishers Limited, part of Springer Nature. All rights reserved.

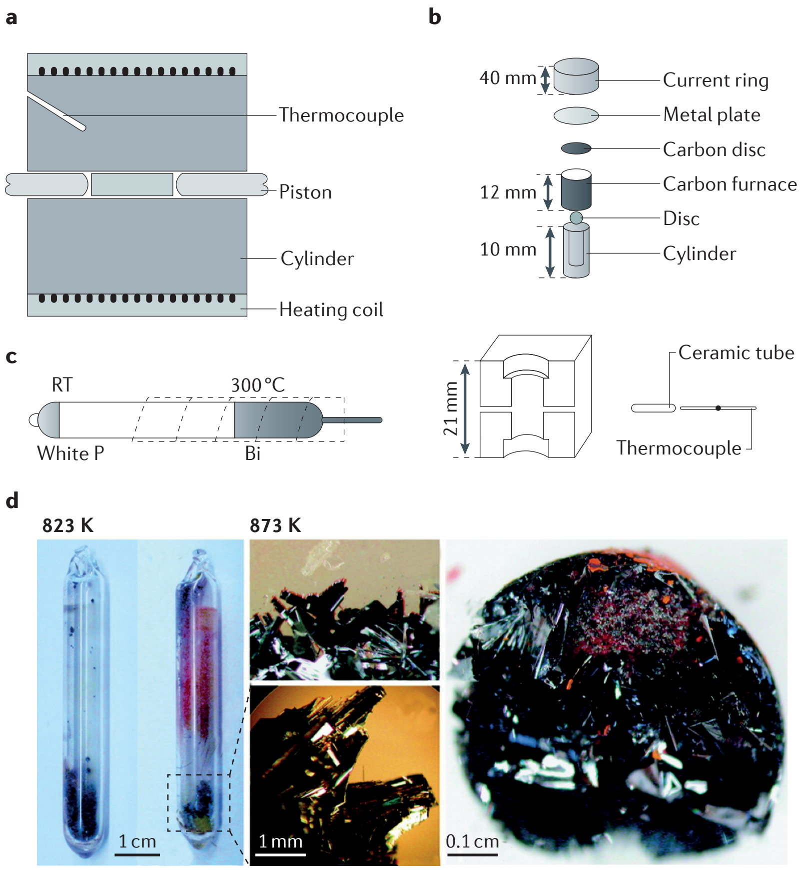

Figure 4 | **Synthesis of black phosphorus.** Schematic illustrations of the experimental setups used for black phosphorus growth. High pressure methods involve using a pressure cylinder with a lead container[4] (panel **a**) or wedge-type anvil high pressure apparatus[127] (panel **b**). An example of a low pressure route is the bismuth-flux method (panel **c**), in which a completely closed quartz-glass ampule is used for the crystallization of black phosphorus[57]. **d** | The reaction of Au, Sn, red phosphorus and SnI$_4$ in a silica ampule is used for the production of black phosphorus[127,58]. The first photograph (left) shows Sn(IV) iodide condensed on top of black phosphorus after thermal decomposition at 1,073 K (as observed in REF. 127). A representative batch of black phosphorus grown on top of a Au$_3$SnP$_7$/AuSn bulk (photograph on the right) shows the mineralization agent SnI$_4$ (orange dots) well separated from the bulk material. RT, room temperature. Part **a** is adapted from REF. 4, with the permission of AIP Publishing. Part **b** is adapted with permission from REF. 127, Taylor Francis. Part **c** is adapted with permission from REF. 57, Japan Society of Applied Physics. Part **d** is adapted with permission from REF. 58, American Chemical Society.

roughness is observed, followed by the formation of bubble-like spots, as seen in atomic force microscope (AFM) images[18,72–74] (FIG. 5a).

The Raman signatures of phosphorene disappear after degradation[18]. However, the presence of the Raman peaks can be quite misleading; because the oxidation proceeds layer by layer, it tends to completely destroy the Raman signal of the top layers, whereas the Raman spectra from the phosphorene underneath appear nearly unperturbed. Chemisorbed oxygen can be directly detected by Fourier transform infrared spectroscopy[73] and by X-ray photoelectron spectroscopy[73,75].

As expected, the oxidation of phosphorene is much faster for few-layer samples than for bulk crystals, on which oxidation seems to remain confined to the outermost layer or layers[75] (FIG. 5b). Oxidation is known to happen in air; however, whether oxygen alone in the absence of water and light can cause detectable (microscopic) degradation is still a matter of debate.

Encapsulation. In order to avoid oxidation, samples and devices can be encapsulated with an inert material. Several methods have been proposed for the passivation of few-layer phosphorene, including encapsulation with BN[76], polymethyl methacrylate (PMMA)[77], and alumina or AlO$_x$ (REFS 73,78), which are deposited by atomic layer deposition.

PMMA is a transparent thermoplastic that is easy to process and has widespread industrial use[79]. Thus, it has been one of the first materials used to encapsulate phosphorene[77]. It is also used in intermediate steps in the passivation with other materials or in the assembly of heterostructures[76]. Other polymers, such as parylene, have also been used for phosphorene encapsulation[18].

Hexagonal (h)-BN is chemically inert, transparent and insulating, and can be exfoliated into monolayers. Black phosphorus encapsulated between h-BN layers is robust to oxidation and exhibits high mobilities. Graphene contacts can also be incorporated to make fully 2D heterostructure transistors[80] using a procedure[76] based on the dry transfer method developed for the preparation of 2D stacked-layer heterostructures[81]. Because graphene is flat, it is possible to completely encapsulate the structure with h-BN, including the edges of phosphorene, from which oxidation may start. This is arguably an ideal encapsulation method; however, the preparation of a complete device requires a week or longer. It also requires the use of expensive equipment, such as gloveboxes.

AlO$_x$ encapsulation using atomic layer deposition is another route for the suppression of degradation[73,78,82]. This technique has been used to encapsulate flexible phosphorus-based transistors that are stable for more than 2 weeks and can resist more than 5,000 bending cycles[82] (FIG. 5c). This encapsulation technique is one of the most promising in terms of industrial application and scalability.

Thickness determination. The measure of the number of layers and, especially, the identification of monolayers for phosphorene is still not as straightforward as it is for graphene. The techniques that are used, or that have been proposed, for the determination of phosphorene thickness include AFM, scanning tunnelling microscopy (STM), transmission electron microscopy (TEM), Raman spectroscopy, optical imaging and interferometry.

AFM and STM are the most straightforward methods, as they provide a height image (see REFS 67,83 for examples of AFM phosphorene monolayer and two-layer height profiles, and REF. 84 for a STM monolayer height profile). However, there is some variability in the AFM thickness measured for layers exfoliated in the liquid phase.

TEM and high-resolution TEM are convenient techniques to evaluate the crystallinity as well as the thickness of phosphorene samples, and to identify monolayers. Several characterization methods

© 2016 Macmillan Publishers Limited, part of Springer Nature. All rights reserved.

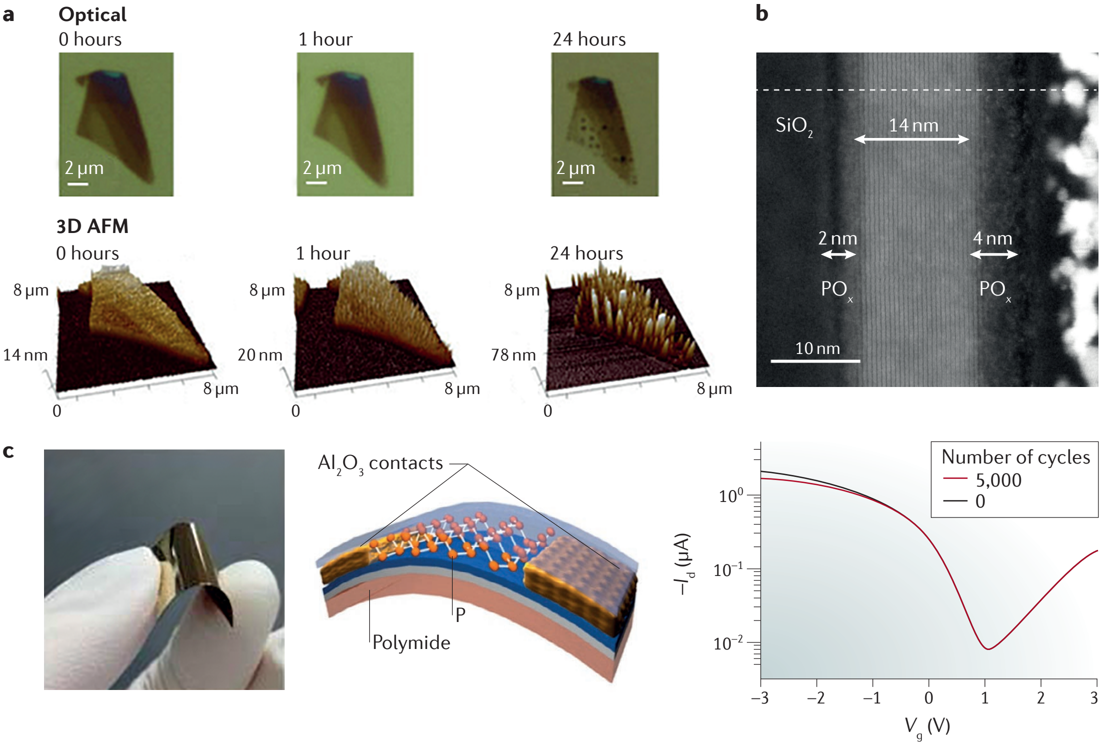

Figure 5 | **Encapsulation of phosphorene for protection against oxidation. a** | Degradation of phosphorene in air imaged with an optical microscope and with an atomic force microscope (AFM) at the indicated times after exfoliation. **b** | Aberration-corrected scanning transmission electron microscope image showing the cross-section of a device in which black phosphorus is covered by oxide layers. **c** | Photograph and schematic representation of a flexible phosphorene-based transistor encapsulated in AlO$_x$ deposited by atomic layer deposition. The graph shows its cyclability against mechanical bending. The characteristic drain current, I_d, versus gate voltage, V_g, is almost unchanged after 5,000 bend cycles. Part **a** is from REF. 78, Nature Publishing Group. Part **b** is adapted with permission from REF. 128, Wiley-VCH. Part **c** is adapted with permission from REF. 82, American Chemical Society.

for phosphorene flakes that use these techniques are described in REF. 85. If the thickness of one of the flakes is known, the thickness of the other flakes can be determined from the contrast using an elastic scattering model[86]. The TEM contrast change across the flake edge can also be used to distinguish the layer number up to four layers. Moreover, in high-resolution TEM, monolayers can be identified by the large 101:200 intensity ratio they show in the fast Fourier transform when imaged at or near the Scherzer defocus (Scherzer defoci and defocus ranges for different microscopes are tabulated in REF. 85). In addition, simulations suggest that for even-layered phosphorus flakes the 101 diffraction spot is absent regardless of the microscope or defocus value, whereas for odd-layered samples other than monolayer, the 101 intensity is severely diminished at or near the Scherzer defocus. Raman spectra can also be used to identify the number of layers based on the Raman peak shift and intensity change[67,83]. However, as we already mentioned, the number of layers cannot be unambiguously determined based on the higher frequency Raman bands only. By contrast, the A_g interlayer vibrational mode in the low-frequency regime shows a large redshift with increasing thickness, two times larger than that for dichalcogenides[87,88]. However, the detection of such low frequencies is not available in all Raman spectrometers.

An alternative interferometry method, consisting of measuring the optical path length of the light reflected from phosphorene mechanically exfoliated onto a SiO$_2$/Si substrate was proposed, because there is a direct relationship between the optical path length and the layer number[38].

Elipsometry has been used to determine the thickness of other 2D materials[89], but it is still not well documented for phosphorene.

Substrate. Most studies on phosphorene use SiO$_2$ as a substrate, because it is cheap, high quality, insulating and transparent. h-BN is another option; because it is atomically smooth and relatively free of charged impurities it gives rise to high carrier mobilities[76]. h-BN also has a high dielectric constant for an insulating material, resulting in a strong damping of the electrostatic repulsion by charged impurities responsible for decreasing the carrier mobility.

Defects and doping

Environmental dopants. One of the most attractive features of phosphorene is that symmetric p- and n-type doping (ambipolar behaviour) can be achieved in FETs by sweeping the gate voltage. However, as-grown black phosphorus is often p-type[46,90] — this may be due to the presence of tin or other unknown dopants introduced during growth.

© 2016 Macmillan Publishers Limited, part of Springer Nature. All rights reserved.

Moreover, for few-layer samples not intentionally doped, there seems to be a relation between the presence of point defects introduced after short exposure to air (even after less than one hour of exposure) and the conductivity type of the samples[74,76]. There has been some speculation in the literature about the contribution of each of the species present in the atmosphere to the modification of the electronic properties of the material and, in particular, to the density of free holes. Here, we consider the effect of some unintentional dopants, shallow donors and acceptors, transfer doping and magnetic species.

The least damaging interaction between phosphorene and atmospheric gas molecules is the physisorption of oxygen and water. The electronic structure of phosphorene is nearly unperturbed by the presence of these defects (FIG. 6a). Water introduces occupied and unoccupied levels in the valence and conduction bands, whereas the lowest unoccupied oxygen minority spin levels lie deep in the middle of the bandgap. This is similar to what happens in graphene, in which the same oxygen minority spin levels lie very close to the Dirac point.

The most stable oxygen point defect is the dangling oxygen (FIG. 6b), which completes the tetrahedral coordination of the nearest phosphorus atom. This defect is electrically neutral. However, another form of this defect — the diagonal oxygen bridge, which is metastable by about 2 eV — acts as an electron trap and potentially as a shallow donor for thicker multilayer samples. This defect seems to be the origin of the electron traps that are introduced during the first hours of exposure to air[76].

Another water-derived dopant is the hydroxyl group, which introduces a semi-filled level in the bandgap, resulting in the formation of donor and acceptor levels (FIG. 6c). However, these levels are in negative-U order, meaning that the neutral charge state is not stable, but the hydroxyl can be found in the negative or positive charge states depending on whether the Fermi level is above or below $E_v + 0.2$ eV, respectively (where E_v is the energy of the top of the valence band). However, if water chemisorption results in hydroxyl and hydrogen adsorbed at neighbouring positions, the hydroxyl gap level is removed from the bandgap, thus there is no net doping.

Hydrogen is a multistable, amphoteric defect; that is, it has both donor and acceptor activity, with levels at $E_v + 0.45$ eV and $E_c - 0.34$ eV, respectively (FIG. 6d, where E_c is the energy of the bottom of the conduction band). The paramagnetic, neutral charge state takes the bond-centred configuration shown at the top of FIG. 6d, whereas positive and negative charge states favour the dangling configuration shown in the bottom schematic of FIG. 6d. Eventually, hydrogenation of phosphorene leads to decomposition[91,92].

Finally, tin has been found at the surface of bulk samples as a spurious contaminant left during growth[75]. Because it has one valence electron less than phosphorus, tin is expected to be a shallow acceptor, but to date, there are no studies confirming its contribution to unintentional doping.

Intentional dopants. Tellurium is known to act as a shallow donor in bulk black phosphorus[90,93], converting p-type samples into n-type samples. Alkali metals, copper and silver have also been found to be shallow donors[94,95]. Lithium, sodium and potassium can occupy both surface and intercalated positions; they donate their *s* electron to the conduction band states, and for low concentrations, they leave the bands nearest to the bandgap nearly undisturbed[95,96]. Copper, adsorbed or intercalated, also donates a single electron per dopant atom; it has been experimentally confirmed that copper deposition is an effective way to obtain n-type conduction in few-layer phosphorene devices[97]. Electron doping has also been achieved by transfer doping with Cs_2CO_3 (REF. 98).

In bulk black phosphorus, doping with potassium not only adds electrons to the system, but it also introduces a transverse electric field that closes the bandgap[95]. This effect has not been observed in thinner few-layer devices, which preserve their semiconducting characteristics when doped[97].

As-grown black phosphorus is usually p-type, but the hole density can be further increased by chemical doping. Different from the same-column elements silver and copper, adsorbed gold atoms were found to be deep electron acceptors[99,100]. Carbon and silicon have also been suggested to be acceptor defects on the basis of numerical calculations[96]. Other methods to increase the hole density include transfer doping with MoO_3 (REF. 98) and surface treatment with aryl diazonium[101]. Phosphorene is thus among the few semiconductors that can be chemically doped to become both p-type or n-type.

Among magnetic dopants, the elements from scandium to zinc have been taken into consideration[99,102–104], with some of them in both the substitutional and adsorbed form. Chromium, which has a spin of nearly $5\mu_B$ when adsorbed at the surface of an intrinsic material, has the highest magnetic moment[103]. Because spin–orbit coupling in phosphorene is not particularly strong, introducing magnetic dopants is one of the most immediate ways to engineer the spin structure of the material.

Intrinsic point defects. Single vacancies and single interstitial defects in phosphorene create dangling bonds, introducing spin-polarized acceptor states within ~0.1 eV from the valence band top[93,105]. The lowest energy vacancies lead to a reconstruction in which the atoms form a pentagon[93], an aspect that has been missed by some research, leading to discording results being reported in the literature. Nonetheless, the lowest energy intrinsic defects are not single vacancies and interstitials. The divacancy, which has a formation energy of 1.36 eV, is 0.27 eV more stable than the single vacancy, indicating that vacancy clustering is favourable. The Stone–Wales defect, a bond-distortion complex, has a formation energy of 1.40 eV (REF. 93). The fact that neither the divacancy nor the Stone–Wales defect, as well as the extended intrinsic defects, introduce states in the bandgap indicates that the electronic properties of phosphorene crystals are quite unperturbed by the presence of intrinsic defects. This is an advantage over TMDCs, in which chalcogen vacancies introduce deep states that are invariably present in pristine material[106].

© 2016 Macmillan Publishers Limited, part of Springer Nature. All rights reserved.

Edges and grain boundaries are also found, in most cases, to be electrically inactive following reconstruction[84,92,93,107].

Devices

Field-effect transistors. The variable bandgap energy, together with the high hole mobility at room temperature (up to 1,000 cm^2 V^{-1} s^{-1} for a thickness of ~10 nm) make phosphorene suitable for electronic and optoelectronic applications[15,17,42,72,108–109]. Most of the device designs proposed so far are based on FETs. FETs with phosphorene channels have consistently high on/off ratios (as high as 10^5)[15,17,72,108]. Subthreshold swings are still high, but a value as low as 69 meV dec^{-1} has been achieved for black phosphorus transistors with a high-k dielectric[110]. By carefully choosing the channel length, dielectric thickness and contacts, it is possible to obtain well-defined saturation of the drain current in the high drain–source bias region[15,111], a desirable characteristic for radio-frequency applications that is lacking in graphene-based transistors[112,113].

The first studies[113] show that phosphorene transistors perform well in the radio-frequency range, exhibiting a peak short-circuit current gain cutoff frequency and a maximum oscillation frequency of 12 GHz and 30 Hz, respectively, for a channel length of 300 nm.

The major challenges so far are the control of the device thickness, the suppression of degradation processes, and the control of the Schottky barrier height and of the conduction type.

Both the spectral response and the mobility depend critically on the number of phosphorene layers. At the same time, because — unlike in other 2D materials — the bandgap is direct (or nearly direct) regardless of the thickness, for most low frequency applications it is a good compromise to use a multilayer channel (with a thickness of ~10 nm), which provides a higher carrier mobility. This results in higher driving currents but in a lower on/off ratio[19,113]. Presently, the control of the channel thickness remains a problem because of the lack of scalable exfoliation methods able to produce samples with a narrow thickness distribution. In this regard, exfoliation in liquid and/or plasma thinning are the most promising solutions.

The other crucial aspect of FET design is the choice of contacts. In 2D heterostructures, the contacts often determine the conduction type and limit the source–drain current[19,80]. Thus, good Ohmic contact materials

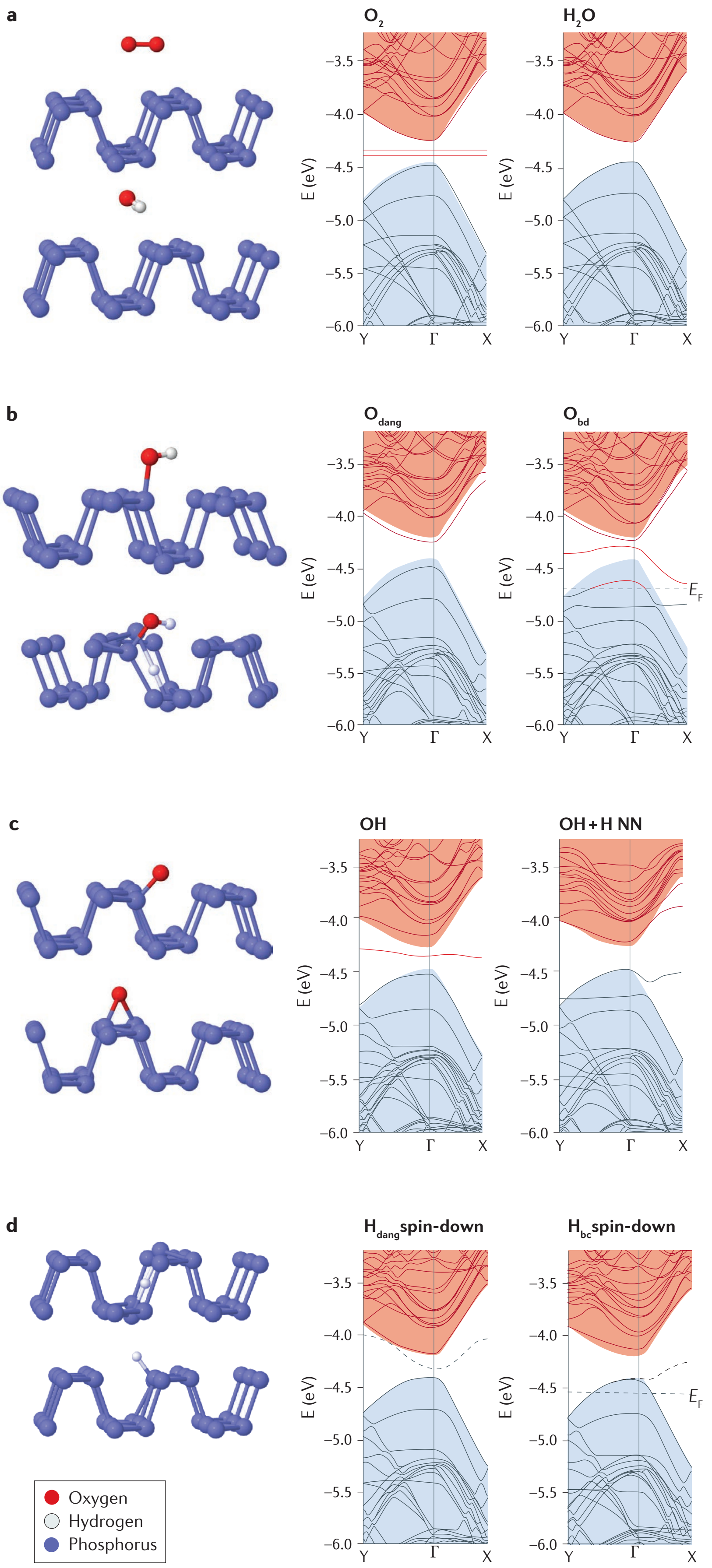

Figure 6 | **Defects in phosphorene.** Schematic diagrams of the adsorption geometry of the dopants and resulting band structures for: physisorbed oxygen and water[129] (part **a**), oxygen defects (part **b**), hydroxyl groups and dissociated water (part **c**), and hydrogen (part **d**). The red and blue shaded areas indicate the band structure of pristine phosphorene. Γ = (0, 0) denotes the centre of the 2D Brillouin zone, and the points X and Y have coordinates (1, 0) and (0, 1), respectively. E, energy; E_F, Fermi level; H$_{bc}$, bond-centred hydrogen; H$_{dang}$, dangling hydrogen; NN, nearest neighbour; O$_{bd}$, diagonal oxygen bridge; O$_{dang}$, dangling oxygen.

© 2016 Macmillan Publishers Limited, part of Springer Nature. All rights reserved.

are needed. TiO_2/Co contacts lead to high Schottky barrier heights in black phosphorus-based devices and, consequently, to a source–drain current dominated by thermionic emission[80,108]. Ti/Au contacts on phosphorene do not result in a linear relation between the source–drain current and the source–drain voltage, even at low biases[80]. By contrast, if graphene is used, the contacts can be made Ohmic by tuning the graphene work function using the gate-modulation effect[80]. A phosphorene-based FET prototype fully encapsulated with h-BN and with graphene contacts is shown in FIG. 7a–c and depicted schematically in FIG. 7d. Its characteristics (source–drain current as a function of back-gate and source–drain bias) are shown in FIG. 7e,f. The transport through the black phosphorus layer is determined by the relative energy alignment of the two graphene contacts (FIG. 7g). Apart from solving the problem of thermionic emission-limited transport, the graphene/black phosphorus combination has the advantage of forming a van der Waals structure that can be fully encapsulated with h-BN (in contrast to black phosphorus with traditional non-flexible contacts, which are not well sealed by h-BN, causing leakages)[80].

Photodetectors. Owing to the tunable bandgap, ranging from infrared to visible frequencies, and to its high absorption coefficient in the UV region, multilayer phosphorene is very well suited for photodetector applications.

Phototransistors with a thick few-layer phosphorene channel can be used for infrared detection in the important near-infrared telecom band[114–117]. In intrinsic conditions, the photovoltaic effect gives rise to absorption in the infrared, with an internal quantum efficiency near 50% and a dark current of only 220 nA, more than three orders of magnitude smaller than that of a graphene photodetector under a similar bias[115]. Phosphorene FETs show a broadband photoresponse from visible up to UV frequencies[30], as seen in the optical spectra simulations in FIG. 2b (REF. 118). The photovoltaic effect has been demonstrated in p–n junctions (created by a split-gate or by ionic-gel gating)[32,116] and FETs[34,117]. Because black phosphorus is ambipolar and the conductivity type can be controlled by field effect, black phosphorus-based optical photodetectors can be operated both in the electron and hole doping regime[117]. The current operating levels in the two regimes are different because of the band alignment imposed by the work function of the contacts. For Ti/Au contacts, the optimal operating conditions are reached in the p-type regime, with a photoresponse of $4.8\,\mathrm{mA\,W^{-1}}$ at visible frequencies and rise and fall times of 1 and 4 ms, respectively[117].

Phosphorene has a high photoresponse in the UV range (above ~5 eV), about one order of magnitude larger than its photoresponse at frequencies close to the absorption edge (FIG. 7h). The same effect is present in bulk samples, and it is a consequence of band-nesting[119], which gives rise to diverging singularities in the absorption spectra of 2D semiconductors. In thick multilayer phosphorene transistors, the high UV response has been observed in optical conductivity measurements[34]; the modulation of the photoresponse current under dark-light conditions is shown in FIG. 7h.

For high doping, it has been proposed that thermoelectric and bolometric effects (arising from the change of electric conductivity with temperature) become particularly important. Thus, for heavily doped samples, the photoinduced thermoelectric effect dominates at low bias, whereas the bolometric effect prevails at high bias[113,120]. The bolometric current generation can be distinguished from the photoelectric current generation by the polarity of the source–drain current with respect to the bias under illumination[114] (FIG. 7i).

Conclusion and outlook

The unusual structure of phosphorene sets it aside from graphene and other widely studied 2D semiconductors. Thus, phosphorene offers many opportunities for the investigation of fundamental phenomena. In the past three years, modern techniques tailored to 2D materials have allowed the isolation and characterization of monolayer and few-layer phosphorene. Some of the remarkable properties of phosphorene, as are highlighted in this Review, include a negative Poisson's ratio, high thermoelectric ZT, high electron and hole mobilities, and superconductivity. Some of these properties, such as superconductivity, have been predicted theoretically and still await experimental verification.

At present, the bottlenecks in the study of phosphorene and in its applications are the limited availability of the material and its fast degradation. Limited availability can only be solved through greater investment in the industrial-scale production of phosphorene, which will no doubt become more desirable as its potential is further unveiled. The fast degradation upon exposure to ambient conditions does not need to be a limiting factor, as proved by the organic light-emitting diode industry, in which encapsulation is a viable and reliable technology. Both known encapsulation techniques (atomic layer deposition of Al_2O_3 or AlO_x and PMMA encapsulation) and novel techniques inspired by graphene research (h-BN and graphene encapsulation in 2D stacked heterostructures) have already been applied to phosphorene with very encouraging results.

Despite these difficulties, few-layer phosphorene can maintain excellent crystal quality after isolation, in laboratory conditions, as testified by the observation of quantum oscillations. Several types of phosphorene-based devices have been demonstrated, and their performance has exceeded the best expectations. FETs exhibit better performances than TMDC FETs in terms of on/off ratio and mobility. In comparison to other 2D materials, phosphorene FETs can provide good mobility, a balanced on/off ratio and a desirable current saturation — the potential is particularly high for radio-frequency applications. In addition, the range of bandgaps — from 0.3 eV (bulk) to 2.0 eV (monolayer) — spans the spectrum from visible to infrared radiation, and has been explored for photodetection. Owing to the anisotropic properties of phosphorene, the angle-resolved electronic transport and the related optical features are also of interest; additionally, angle-resolved infrared and Raman spectroscopy

© 2016 Macmillan Publishers Limited, part of Springer Nature. All rights reserved.

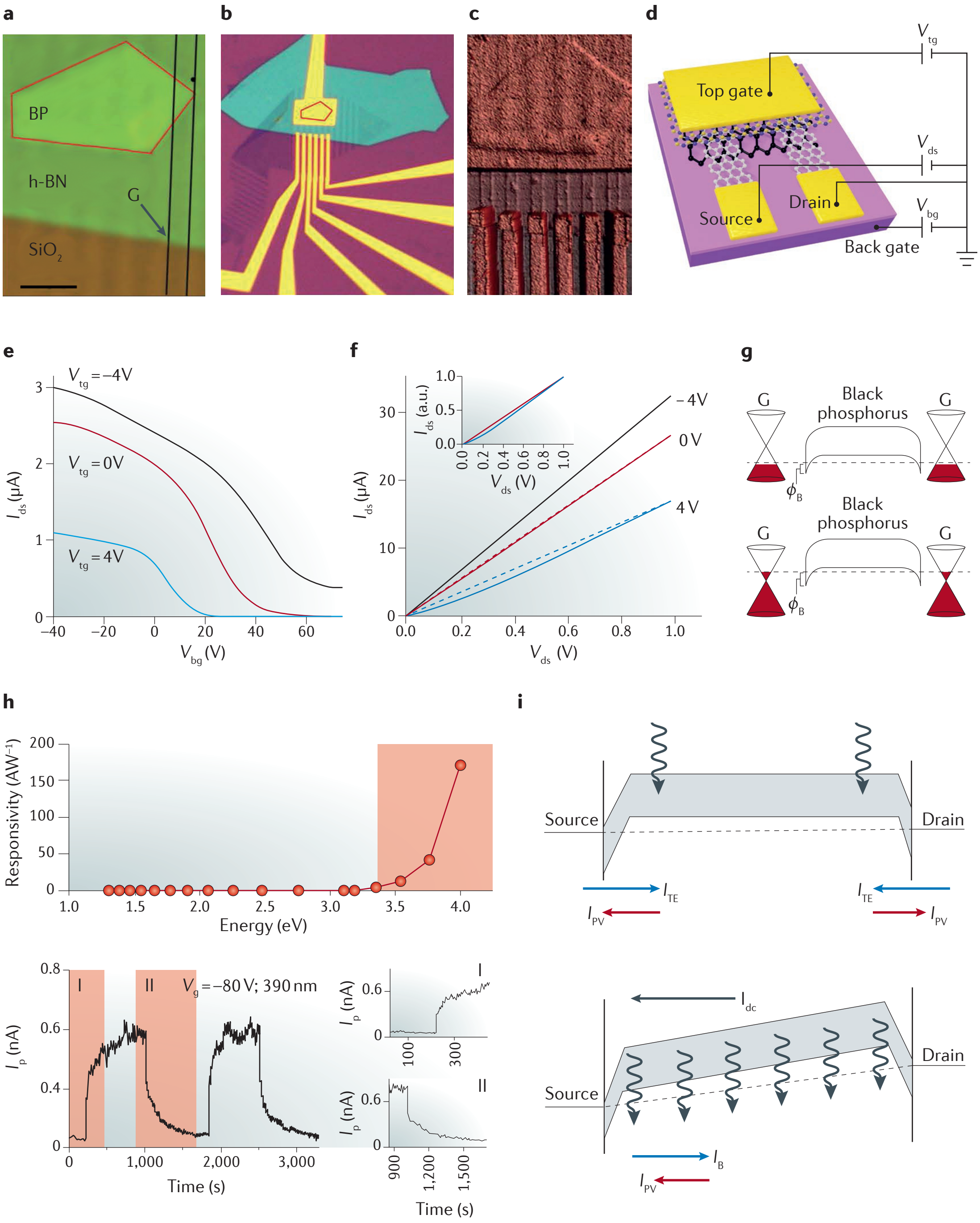

Figure 7 | **Phosphorene-based devices. a–g** | Phosphorene-based field-effect transistor (with 4.5-nm-thick phosphorus), contacted with graphene (G) and encapsulated with hexagonal boron nitride (h-BN), showing an optical image of the device after the final transfer process (part **a**). Red and black areas show the black phosphorus (BP) crystal and one of the graphene stripes, respectively. **b** | Optical image of the device after the contacts are formed. **c** | Atomic force microscopy image of the device. **d** | Schematic diagram of a graphene-contacted phosphorene device. **e** | Back-gate voltage (V_{bg}) dependence of the drain–source current (I_{ds}) at different top-gate voltage values (V_{tg}). **f** | Drain–source voltage (V_{ds}) dependence of the bias current at different displacement fields. The bottom gate voltage is fixed to −30 V. The inset shows the same curves normalized to one. **g** | The top and bottom schematics illustrate the band alignment for V_{tg} values of −4 and 4 V, respectively, at fixed V_{bg} = −30 V. **h** | Phosphorene-based UV photodetector photoresponsivity and photocurrent under illumination. The regions denoted I and II are dark intervals[32]. **i** | Band diagram of a phosphorene-based phototransistor at zero and finite bias. The polarity of photocurrents, *I*, of different origin is highlighted: thermoelectric (TE), bolometric (B) and photovoltaic (PV). φ_B, graphene work function; I_{dc}, dark current; I_p, photocurrent. Parts **a**–**g** are adapted with permission from REF. 80, American Chemical Society. Part **h** is adapted with permission from REF. 32, American Chemical Society. Part **i** is adapted with permission from REF. 120, American Physical Society.

© 2016 Macmillan Publishers Limited, part of Springer Nature. All rights reserved.

can determine the direction of phosphorene crystals, increasing the quality of device fabrication.

Black phosphorus provides many opportunities for further band structure engineering and, combined with other materials, for the design of 2D heterostructure devices. Based on the theoretical works available to date, there are still properties and models that require verification, which include: a clarification of the optical and transport bandgaps of monolayer phosphorene; direct band structure (ARPES) measurements for few-layer phosphorene; the detection of higher exciton states; the confirmation of the dominant factors limiting electron and hole mobility, and the measurement of the upper bound for the phonon-limited carrier mobility in few-layer samples; the identification and imaging of low-angle edge defects; and, finally, the observation of magnetism and superconductivity. We hope this Review inspires more dramatic discoveries, both in the physics and in the applications of this remarkable material.

1. Corbridge, D. *Phosphorus: Chemistry, Biochemistry and Technology* 6th edn (CRC Press, 2013).
2. Bridgman, P. W. Two new modifications of phosphorus. *J. Am. Chem. Soc.* **36**, 1344–1363 (1914).
3. Bridgman, P. W. Further note on black phosphorus. *J. Am. Chem. Soc.* **38**, 609–612 (1916).
4. Jacobs, R. B. Phosphorus at high temperatures and pressures. *J. Chem. Phys.* **5**, 945–953 (1937).
5. Keyes, R. W. The electrical properties of black phosphorus. *Phys. Rev.* **92**, 580–584 (1953).
6. Greenwood, N. N. & Earnshaw, A. (eds) *Chemistry of the Elements* (Elsevier, 2012).
7. Zhu, Z. & Tománek, D. Semiconducting layered blue phosphorus: a computational study. *Phys. Rev. Lett.* **112**, 176802 (2014).
8. Guo, H., Lu, N., Dai, J., Wu, X. & Zeng, X. C. Phosphorene nanoribbons, phosphorus nanotubes, and van der Waals multilayers. *J. Phys. Chem. C* **118**, 14051–14059 (2014).
9. Guan, J., Zhu, Z. & Tománek, D. Phase coexistence and metal–insulator transition in few-layer phosphorene: a computational study. *Phys. Rev. Lett.* **113**, 046804 (2014).
10. Wittig, J. & Matthias, B. T. Superconducting phosphorus. *Science* **160**, 994–995 (1968).
11. Rajagopalan, M., Alouani, M. & Christensen, N. Calculation of band structure and superconductivity in the simple cubic phase of phosphorus. *J. Low Temp. Phys.* **75**, 1–13 (1989).
12. Chan, K. T., Malone, B. D. & Cohen, M. L. Pressure dependence of superconductivity in simple cubic phosphorus. *Phys. Rev. B* **88**, 064517 (2013).
13. Karuzawa, M., Ishizuka, M. & Endo, S. The pressure effect on the superconducting transition temperature of black phosphorus. *J. Phys. Condens. Matter* **14**, 10759 (2002).
14. Kawamura, H., Shirotani, I. & Tachikawa, K. Anomalous superconductivity and pressure induced phase transitions in black phosphorus. *Solid State Commun.* **54**, 775–778 (1985).
15. Li, L. *et al.* Black phosphorus field-effect transistors. *Nat. Nanotechnol.* **9**, 372–377 (2014).
16. Rodin, A. S., Carvalho, A. & Castro Neto, A. H. Strain-induced gap modification in black phosphorus. *Phys. Rev. Lett.* **112**, 176801 (2014).
17. Liu, H. *et al.* Phosphorene: an unexplored 2D semiconductor with a high hole mobility. *ACS Nano* **8**, 4033–4041 (2014).
18. Favron, A. *et al.* Photooxidation and quantum confinement effects in exfoliated black phosphorus. *Nat. Mater.* **14**, 826–832 (2015).
19. Liu, H., Du, Y., Deng, Y. & Ye, P. D. Semiconducting black phosphorus: synthesis, transport properties and electronic applications. *Chem. Soc. Rev.* **44**, 2732–2743 (2015).
20. Ling, X., Wang, H., Huang, S., Xia, F. & Dresselhaus, M. S. The renaissance of black phosphorus. *Proc. Natl Acad. Sci. USA* **112**, 4523–4530 (2015).
21. Ryder, C. R., Wood, J. D., Wells, S. A. & Hersam, M. C. Chemically tailoring semiconducting two-dimensional transition metal dichalcogenides and black phosphorus. *ACS Nano* **10**, 3900–3917 (2016).
22. Pauling, L. & Simonetta, M. Bond orbitals and bond energy in elementary phosphorus. *J. Chem. Phys.* **20**, 29–34 (1952).
23. Hart, R. R., Robin, M. B. & Kuebler, N. A. 3*p* orbitals, bent bonds, and the electronic spectrum of the P_4 molecule. *J. Chem. Phys.* **42**, 3631–3638 (1965).
24. Hulliger, F. *Physics and Chemistry of Layered Materials* Vol. 5 (Reidel, 1977).
25. Cartz, L., Srinivasa, S. R., Riedner, R. J., Jorgensen, J. D. & Worlton, T. G. Effect of pressure on bonding in black phosphorus. *J. Chem. Phys.* **71**, 1718–1721 (1979).
26. Qiao, J., Kong, X., Hu, Z.-X., Yang, F. & Ji, W. High-mobility transport anisotropy and linear dichroism in few-layer black phosphorus. *Nat. Commun.* **5**, 4475 (2014).
27. Jiang, J.-W. & Park, H. S. Negative Poisson's ratio in single-layer black-phosphorus. *Nat. Commun.* **5**, 4727 (2014).
28. Tran, V., Soklaski, R., Liang, Y. & Yang, L. Layer-controlled band gap and anisotropic excitons in few-layer black phosphorus. *Phys. Rev. B* **89**, 235319 (2014).
29. Li, P. & Appelbaum, I. Electrons and holes in phosphorene. *Phys. Rev. B* **90**, 115439 (2014).
30. Yuan, H. *et al.* Polarization-sensitive broadband photodetector using a black phosphorus vertical p–n junction. *Nat. Nanotechnol.* **10**, 707–713 (2015).
31. Low, T. *et al.* Tunable optical properties of multilayer black phosphorus thin films. *Phys. Rev. B* **90**, 075434 (2014).
32. Wu, J. *et al.* Colossal ultraviolet photoresponsivity of few-layer black phosphorus. *ACS Nano* **9**, 8070–8077 (2015).
33. Wang, X. *et al.* Highly anisotropic and robust excitons in monolayer black phosphorus. *Nat. Nanotechnol.* **10**, 517–521 (2015).
34. Rodin, A. S., Carvalho, A. & Castro Neto, A. H. Excitons in anisotropic two-dimensional semiconducting crystals. *Phys. Rev. B* **90**, 075429 (2014).
35. Rohlfing, M. & Louie, S. G. Electron–hole excitations and optical spectra from first principles. *Phys. Rev. B* **62**, 4927–4944 (2000).
36. Wirtz, L., Marini, A. & Rubio, A. Excitons in boron nitride nanotubes: dimensionality effects. *Phys. Rev. Lett.* **96**, 126104 (2006).
37. Zhang, S. *et al.* Extraordinary photoluminescence and strong temperature/angle-dependent Raman responses in few-layer phosphorene. *ACS Nano* **8**, 9590–9596 (2014).
38. Yang, J. *et al.* Unambiguous identification of monolayer phosphorene by phase-shifting interferometry. Preprint at https://arxiv.org/abs/1412.6701 (2014).
39. Yang, J. *et al.* Optical tuning of exciton and trion emissions in monolayer phosphorene. *Light Sci. Appl.* **4**, e312 (2015).
40. Castellanos-Gomez, A. *et al.* Isolation and characterization of few-layer black phosphorus. *2D Mater.* **1**, 025001 (2014).
41. Li, L. *et al.* Quantum oscillations in a two-dimensional electron gas in black phosphorus thin films. *Nat. Nanotechnol.* **10**, 608–613 (2015).
42. Gillgren, N. *et al.* Gate tunable quantum oscillations in air-stable and high mobility few-layer phosphorene heterostructures. *2D Mater.* **2**, 011001 (2015).
43. Ribeiro-Soares, J., Almeida, R. M., Cançado, L. G., Dresselhaus, M. S. & Jorio, A. Group theory for structural analysis and lattice vibrations in phosphorene systems. *Phys. Rev. B* **91**, 205421 (2015).
44. Sugai, S. & Shirotani, I. Raman and infrared reflection spectroscopy in black phosphorus. *Solid State Commun.* **53**, 753–755 (1985).
45. Fei, R. & Yang, L. Strain-engineering the anisotropic electrical conductance of few-layer black phosphorus. *Nano Lett.* **14**, 2884–2889 (2014).
46. Flores, E. *et al.* Thermoelectric power of bulk black-phosphorus. *Appl. Phys. Lett.* **106**, 022102 (2015).
47. Fei, R. *et al.* Enhanced thermoelectric efficiency via orthogonal electrical and thermal conductances in phosphorene. *Nano Lett.* **14**, 6393–6399 (2014).
48. Jang, H., Wood, J. D., Ryder, C. R., Hersam, M. C. & Cahill, D. G. Anisotropic thermal conductivity of exfoliated black phosphorus. *Adv. Mater.* **27**, 8017–8022 (2015).
49. Luo, Z. *et al.* Anisotropic in-plane thermal conductivity observed in few-layer black phosphorus. *Nat. Commun.* **6**, 8572 (2015).
50. Lv, H., Lu, W., Shao, D. & Sun, Y. Large thermoelectric power factors in black phosphorus and phosphorene. Preprint at https://arxiv.org/abs/1404.5171 (2014).
51. Zhang, J. *et al.* Phosphorene nanoribbon as a promising candidate for thermoelectric applications. *Sci. Rep.* **4**, 6452 (2014).
52. Wu, H. *et al.* Broad temperature plateau for thermoelectric figure of merit $ZT > 2$ in phase-separated $PbTe_{0.7}S_{0.3}$. *Nat. Commun.* **5**, 4515 (2014).
53. Kawamura, H., Shirotani, I. & Tachikawa, K. Anomalous superconductivity in black phosphorus under high pressures. *Solid State Commun.* **49**, 879–881 (1984).
54. Shao, D. F., Lu, W. J., Lv, H. Y. & Sun, Y. P. Electron-doped phosphorene: a potential monolayer superconductor. *Europhys. Lett.* **108**, 67004 (2014).
55. Huang, G. Q., Xing, Z. W. & Xing, D. Y. Prediction of superconductivity in Li-intercalated bilayer phosphorene. *Appl. Phys. Lett.* **106**, 113107 (2015).
56. Bridgman, P. W. The compressibility and pressure coefficient of resistance of ten elements. *Proc. Am. Acad. Arts Sci.* **76**, 55–70 (1948).
57. Baba, M., Izumida, F., Takeda, Y. & Morita, A. Preparation of black phosphorus single crystals by a completely closed bismuth-flux method and their crystal morphology. *Jpn. J. Appl. Phys.* **28**, 1019 (1989).
58. Lange, S., Schmidt, P. & Nilges, T. Au_3SnP_7@Black phosphorus: an easy access to black phosphorus. *Inorg. Chem.* **46**, 4028–4035 (2007).
59. Nilges, T., Kersting, M. & Pfeifer, T. A fast low-pressure transport route to large black phosphorus single crystals. *J. Solid State Chem.* **181**, 1707–1711 (2008).
60. Sansone, G., Maschio, L., Usvyat, D., Schtz, M. & Karttunen, A. Toward an accurate estimate of the exfoliation energy of black phosphorus: a periodic quantum chemical approach. *J. Phys. Chem. Lett.* **7**, 131–136 (2015).
61. Shulenburger, L., Baczewski, A., Zhu, Z., Guan, J. & Tománek, D. The nature of the interlayer interaction in bulk and few-layer phosphorus. *Nano Lett.* **15**, 8170–8175 (2015).
62. Yasaei, P. *et al.* High-quality black phosphorus atomic layers by liquid-phase exfoliation. *Adv. Mater.* **27**, 1887–1892 (2015).
63. Brent, J. R. *et al.* Production of few-layer phosphorene by liquid exfoliation of black phosphorus. *Chem. Commun.* **50**, 13338–13341 (2014).
64. Kang, J. *et al.* Solvent exfoliation of electronic-grade, two-dimensional black phosphorus. *ACS Nano* **9**, 3596–3604 (2015).
65. Sotor, J. *et al.* Ultrafast thulium-doped fiber laser mode locked with black phosphorus. *Opt. Lett.* **40**, 3885–3888 (2015).
66. Kang, J. *et al.* Stable aqueous dispersions of optically and electronically active phosphorene. Preprint at https://arxiv.org/abs/1604.05677 (2016).
67. Lu, W. *et al.* Plasma-assisted fabrication of monolayer phosphorene and its Raman characterization. *Nano Res.* **7**, 853–859 (2014).
68. Ziletti, A. *et al.* Phosphorene oxides: bandgap engineering of phosphorene by oxidation. *Phys. Rev. B* **91**, 085407 (2015).
69. Ziletti, A., Carvalho, A., Campbell, D. K., Coker, D. F. & Castro Neto, A. H. Oxygen defects in phosphorene. *Phys. Rev. Lett.* **114**, 046801 (2015).

© 2016 Macmillan Publishers Limited, part of Springer Nature. All rights reserved.

70. Utt, K. L. *et al.* Intrinsic defects, fluctuations of the local shape, and the photo-oxidation of black phosphorus. *ACS Cent. Sci.* **1**, 320–327 (2015).
71. Yang, T. *et al.* Interpreting core-level spectra of oxidizing phosphorene: theory and experiment. *Phys. Rev. B* **92**, 125412 (2015).
72. Koenig, S. P., Doganov, R. A., Schmidt, H., Castro Neto, A. H. & Ozyilmaz, B. Electric field effect in ultrathin black phosphorus. *Appl. Phys. Lett.* **104**, 103106 (2014).
73. Wood, J. D. *et al.* Effective passivation of exfoliated black phosphorus transistors against ambient degradation. *Nano Lett.* **14**, 6964–6970 (2014).
74. Island, J. O., Steele, G. A., van der Zant, H. S. J. & Castellanos-Gomez, A. Environmental instability of few-layer black phosphorus. *2D Mater.* **2**, 011002 (2015).
75. Edmonds, M. T. *et al.* Creating a stable oxide at the surface of black phosphorus. *ACS Appl. Mater. Interfaces* **7**, 14557–14562 (2015).
76. Doganov, R. A. *et al.* Transport properties of ultrathin black phosphorus on hexagonal boron nitride. *Appl. Phys. Lett.* **106**, 083505 (2015).
77. Tayari, V. *et al.* Two-dimensional magnetotransport in a black phosphorus naked quantum well. *Nat. Commun.* **6**, 7702 (2015).
78. Kim, J.-S. *et al.* Toward air-stable multilayer phosphorene thin-films and transistors. *Sci. Rep.* **5**, 8989 (2015).
79. Mittal, V. *Encapsulation Nanotechnologies* (Wiley, 2013).
80. Avsar, A. *et al.* Air-stable transport in graphene-contacted, fully encapsulated ultrathin black phosphorus-based field-effect transistors. *ACS Nano* **9**, 4138–4145 (2015).
81. Dean, C. R. *et al.* Boron nitride substrates for high-quality graphene electronics. *Nat. Nanotechnol.* **5**, 722–726 (2010).
82. Zhu, W. *et al.* Flexible black phosphorus ambipolar transistors, circuits and AM demodulator. *Nano Lett.* **15**, 1883–1890 (2015).
83. Guo, Z. *et al.* From black phosphorus to phosphorene: basic solvent exfoliation, evolution of raman scattering, and applications to ultrafast photonics. *Adv. Funct. Mater.* **25**, 6996–7002 (2015).
84. Liang, L. *et al.* Electronic bandgap and edge reconstruction in phosphorene materials. *Nano Lett.* **14**, 6400–6406 (2014).
85. Woomer, A. H. *et al.* Phosphorene: synthesis, scale-up, and quantitative optical Spectroscopy. *ACS Nano* **9**, 8869–8884 (2015).
86. Liu, X., Wood, J. D., Chen, K.-S., Cho, E. & Hersam, M. C. *In situ* thermal decomposition of exfoliated two-dimensional black phosphorus. *J. Phys. Chem. Lett.* **6**, 773–778 (2015).
87. Luo, X. *et al.* Large frequency change with thickness in interlayer breathing mode: significant interlayer interactions in few layer black phosphorus. *Nano Lett.* **15**, 3931–3938 (2015).
88. Ling, X. *et al.* Low-frequency interlayer breathing modes in few-layer black phosphorus. *Nano Lett.* **15**, 4080–4088 (2015).
89. Weber, J., Calado, V. & Van de Sanden, M. Optical constants of graphene measured by spectroscopic ellipsometry. *Appl. Phys. Lett.* **97**, 091904 (2010).
90. Morita, A. Semiconducting black phosphorus. *Appl. Phys. A* **39**, 227–242 (1986).
91. Boukhvalov, D. W., Rudenko, A. N., Prishchenko, D. A., Mazurenko, V. G. & Katsnelson, M. I. Chemical modifications and stability of phosphorene with impurities: a first principles study. *Phys. Chem. Chem. Phys.* **17**, 15209–15217 (2015).
92. Carvalho, A., Rodin, A. S. & Neto, A. H. C. Phosphorene nanoribbons. *Europhys. Lett.* **108**, 47005 (2014).
93. Liu, Y., Xu, F., Zhang, Z., Penev, E. S. & Yakobson, B. I. Two-dimensional mono-elemental semiconductor with electronically inactive defects: the case of phosphorus. *Nano Lett.* **14**, 6782–6786 (2014).
94. Kulish, V. V., Malyi, O. I., Persson, C. & Wu, P. Adsorption of metal adatoms on single-layer phosphorene. *Phys. Chem. Chem. Phys.* **17**, 992–1000 (2015).
95. Kim, J. *et al.* Observation of tunable band gap and anisotropic dirac semimetal state in black phosphorus. *Science* **349**, 723–726 (2015).
96. Liu, X., Wen, Y., Chen, Z., Shan, B. & Chen, R. A first-principles study of sodium adsorption and diffusion on phosphorene. *Phys. Chem. Chem. Phys.* **17**, 16398–16404 (2015).
97. Koenig, S. P. *et al.* Electron doping of ultrathin black phosphorus with Cu adatoms. *Nano Lett.* **16**, 2145–2151 (2016).
98. Xiang, D. *et al.* Surface transfer doping induced effective modulation on ambipolar characteristics of few-layer black phosphorus. *Nat. Commun.* **6**, 6485 (2015).
99. Hu, T. & Hong, J. First-principles study of metal adatom adsorption on black phosphorene. *J. Phys. Chem. C* **119**, 8199–8207 (2015).
100. Kulish, V. V., Malyi, O. I., Persson, C. & Wu, P. Phosphorene as an anode material for Na-ion batteries: a first-principles study. *Phys. Chem. Chem. Phys.* **17**, 13921–13928 (2015).
101. Ryder, C. R. *et al.* Covalent functionalization and passivation of exfoliated black phosphorus via aryl diazonium chemistry. *Nat. Chem.* **8**, 597–602 (2016).
102. Seixas, L., Carvalho, A. & Castro Neto, A. H. Atomically thin dilute magnetism in Co-doped phosphorene. *Phys. Rev. B* **91**, 155138 (2015).
103. Sui, X. *et al.* Tunable magnetism in transition-metal-decorated phosphorene. *J. Phys. Chem. C* **119**, 10059–10063 (2015).
104. Yu, W. *et al.* Dilute magnetic semiconductor and half metal behaviors in 3d transition-metal doped black and blue phosphorenes: a first-principles study. *Nanoscale Res. Lett.* **11**, 77 (2016).
105. Hu, W. & Yang, J. Defects in phosphorene. *J. Phys. Chem. C* **119**, 20474–20480 (2015).
106. Lu, J. *et al.* Bandgap engineering of phosphorene by laser oxidation toward functional 2D materials. *ACS Nano* **9**, 10411–10421 (2015).
107. Ramasubramaniam, A. & Muniz, A. R. *Ab initio* studies of thermodynamic and electronic properties of phosphorene nanoribbons. *Phys. Rev. B* **90**, 085424 (2014).
108. Venkata Kamalakar, M., Madhushankar, B. N., Dankert, A. & Dash, S. P. Engineering Schottky barrier in black phosphorus field effect devices for spintronic applications. Preprint at https://arxiv.org/abs/1406.4476 (2014).
109. Das, S. *et al.* Tunable transport gap in phosphorene. *Nano Lett.* **14**, 5733–5739 (2014).
110. Liu, X. *et al.* Black phosphorus based field effect transistors with simultaneously achieved near ideal subthreshold swing and high hole mobility at room temperature. *Sci. Rep.* **6**, 24920 (2016).
111. Xia, F., Wang, H. & Jia, Y. Rediscovering black phosphorus as an anisotropic layered material for optoelectronics and electronics. *Nat. Commun.* **5**, 4458 (2014).
112. Palacios, T., Hsu, A. & Wang, H. Applications of graphene devices in RF communications. *IEEE Commun. Mag.* **48**, 122–128 (2010).
113. Wang, H. *et al.* Black phosphorus radio-frequency transistors. *Nano Lett.* **14**, 6424–6429 (2014).
114. Engel, M., Steiner, M. & Avouris, P. Black phosphorus photodetector for multispectral, high-resolution imaging. *Nano Lett.* **14**, 6414–6417 (2014).
115. Youngblood, N., Chen, C., Koester, S. J. & Li, M. Waveguide-integrated black phosphorus photodetector with high responsivity and low dark current. *Nat. Photonics* **9**, 247–252 (2015).
116. Buscema, M., Groenendijk, D. J., Steele, G. A., van der Zant, H. S. J. & Castellanos-Gomez, A. Photovoltaic effect in few-layer black phosphorus PN junctions defined by local electrostatic gating. *Nat. Commun.* **5**, 4651 (2014).
117. Buscema, M. *et al.* Fast and broadband photoresponse of few-layer black phosphorus field-effect transistors. *Nano Lett.* **14**, 3347–3352 (2014).
118. Lin, J.-H., Zhang, H. & Cheng, X.-L. First-principle study on the optical response of phosphorene. *Front. Phys.* **10**, 1–9 (2015).
119. Carvalho, A., Ribeiro, R. M. & Castro Neto, A. H. Band nesting and the optical response of two-dimensional semiconducting transition metal dichalcogenides. *Phys. Rev. B* **88**, 115205 (2013).
120. Low, T., Engel, M., Steiner, M. & Avouris, P. Origin of photoresponse in black phosphorus phototransistors. *Phys. Rev. B* **90**, 081408 (2014).
121. Wu, R. J. *et al.* Atomic and electronic structure of exfoliated black phosphorus. *J. Vacuum Sci. Technol. A* **33**, 060604 (2015).
122. Chernikov, A. *et al.* Exciton binding energy and nonhydrogenic Rydberg series in monolayer WS_2. *Phys. Rev. Lett.* **113**, 076802 (2014).
123. Heremans, J. P., Dresselhaus, M. S., Bell, L. E. & Morelli, D. T. When thermoelectrics reached the nanoscale. *Nat. Nanotechnol.* **8**, 471–473 (2013).
124. Ding, G., Gao, G. & Yao, K. High-efficient thermoelectric materials: the case of orthorhombic IV–VI compounds. *Sci. Rep.* **5**, 9567 (2015).
125. Perdew, J. P. *et al.* Restoring the density-gradient expansion for exchange in solids and surfaces. *Phys. Rev. Lett.* **100**, 136406 (2008).
126. Cai, Y. *et al.* Giant phononic anisotropy and unusual anharmonicity of phosphorene: interlayer coupling and strain engineering. *Adv. Funct. Mater.* **25**, 2230–2236 (2015).
127. Shirotani, I. Growth of large single crystals of black phosphorus at high pressures and temperatures, and its electrical properties. *Mol. Cryst. Liq. Cryst.* **86**, 203–211 (1982).
128. Tian, H. *et al.* Anisotropic black phosphorus synaptic device for neuromorphic applications. *Adv. Mater.* **28**, 4991–4997 (2016).
129. Han, C. *et al.* Strongly modulated ambipolar characteristics of few-layer black phosphorus in oxygen. Preprint at http://arxiv.org/abs/1603.02799 (2016).
130. Novoselov, K. S. *et al.* Two-dimensional atomic crystals. *Proc. Natl Acad. Sci. USA* **102**, 10451–10453 (2005).
131. Du, X., Skachko, I., Barker, A. & Andrei, E. Y. Approaching ballistic transport in suspended graphene. *Nat. Nanotechnol.* **3**, 491–495 (2008).
132. Ellis, J. K., Lucero, M. J. & Scuseria, G. E. The indirect to direct band gap transition in multilayered MoS_2 as predicted by screened hybrid density functional theory. *Appl. Phys. Lett.* **99**, 261908 (2011).
133. Jin, Z., Li, X., Mullen, J. T. & Kim, K. W. Intrinsic transport properties of electrons and holes in monolayer transition-metal dichalcogenides. *Phys. Rev. B* **90**, 045422 (2014).
134. Watanabe, K., Taniguchi, T. & Kanda, H. Direct-bandgap properties and evidence for ultraviolet lasing of hexagonal boron nitride single crystal. *Nat. Mater.* **3**, 404–409 (2004).

Acknowledgements

M.W. acknowledges the financial support from the National Natural Science Foundation of China (Grant No. 21203154). Work at NTU was supported in part by Air Force Office of Scientific Research (Grant no. AFRLAFOSR/AOARD 134074), MOE Tier-2 grant (no. MOE2013-T2-2-049), and A*STAR SERC Grant (no. 1121202012). A.C., A.S.R. and A.H.C.N. were supported by the National Research Foundation, Prime Minister Office, Singapore, under its Medium Sized Centre Programme and CRP award “Novel 2D materials with tailored properties: beyond graphene” (Grant number R-144-000-295-281).

Competing interests statement

The authors declare no competing interests.

SUPPLEMENTARY INFORMATION

See online article: S1 (table) | S2 (table) | S3 (table) | S4 (table)

ALL LINKS ARE ACTIVE IN THE ONLINE PDF

© 2016 Macmillan Publishers Limited, part of Springer Nature. All rights reserved.